



ARTICLE OPEN

Spatiotemporal profiling reveals distinct dynamics and checkpoint regulations of CAR-T and CAR-NKT cells against solid tumors

Yan-Ruide Li^{1,2}, Miao Li^{1,2}, Yuning Chen^{1,2}, Houfu Leng³, Yichen Zhu^{1,2}, Xinyuan Shen^{1,2}, Duncan Croll⁴, Enbo Zhu^{1,2}, Jie Huang^{1,2}, Yu-Chen Wang⁵, Abigail S. Krall³, Heather R. Christofk³, Aldons J. Lusis^{1,6,7} and Lili Yang^{1,2,8,9,10,11,12}

Chimeric antigen receptor (CAR)-engineered T (CAR-T) cell therapies have demonstrated remarkable efficacy in hematologic malignancies; however, their clinical performance in solid tumors remains limited due to suboptimal tumor infiltration, antigen heterogeneity, and immunosuppressive tumor microenvironments (TME). Invariant natural killer T (NKT) cells have recently emerged as a promising alternative platform for CAR engineering, owing to their intrinsic tissue-homing capacity, multi-modal cytotoxicity, and ability to reshape the TME. In this study, we performed a comprehensive preclinical comparison of conventional CAR-T cells and allogeneic stem cell-derived IL-15-enhanced CAR-NKT cells in solid tumor models, integrating spatiotemporal transcriptomic profiling across multiple tissues and longitudinal time points. Our analyses revealed distinct *in vivo* pharmacokinetic, pharmacodynamic, and immunoregulatory profiles between the two cell therapy modalities. Compared with CAR-T cells, CAR-NKT cells demonstrated superior homing, infiltration, and localization within solid tumors, along with prolonged *in vivo* persistence and a unique immune checkpoint receptor expression landscape. Notably, CAR-T cells exhibited synergistic antitumor responses when combined with TIGIT blockade, whereas CAR-NKT cells showed greater sensitivity to CD96 blockade *in vivo*. These findings highlight the divergent therapeutic dynamics of CAR-T and CAR-NKT cells and provide mechanistic insights that inform the rational design of next-generation cell therapies and combinatorial strategies for solid tumors.

Signal Transduction and Targeted Therapy (2026)11:92

; <https://doi.org/10.1038/s41392-026-02602-x>

INTRODUCTION

Chimeric antigen receptor (CAR)-engineered T (CAR-T) cell therapy has revolutionized the treatment of hematologic malignancies, with seven the United States Food and Drug Administration (US FDA)-approved products demonstrating high remission rates in diseases such as B-cell leukemia, lymphoma, and multiple myeloma. However, CAR-T cell therapy faces persistent limitations in solid tumors due to poor tumor infiltration, antigen heterogeneity, and immune suppression within the tumor microenvironment (TME).^{1,2} Invariant natural killer T (NKT) cells have recently emerged as a platform for cell therapy. CAR-NKT cells possess several therapeutic advantages, including the capacity for multi-modal cytotoxicity mediated by CARs, endogenous TCRs, and natural killer receptors (NKR), as well as enhanced tissue homing and tumor infiltration.^{3–5} Notably, CAR-NKT cells exhibit the ability to modulate the immunosuppressive TME by targeting and depleting CD1d⁺ tumor-associated macrophages (TAMs) and

myeloid-derived suppressor cells (MDSCs) via TCR-dependent mechanisms.^{6,7} Currently, both CAR-T and CAR-NKT cell therapies have demonstrated promising therapeutic efficacy against solid tumors in clinical trials. However, the mechanistic and temporal distinctions between these two modalities remain insufficiently characterized, posing challenges to the rational design of clinical applications and combination strategies.

Recent studies suggest that CAR-NKT and CAR-T cells differ markedly in their *in vivo* pharmacokinetics and biodistribution. For example, an allogeneic CD33-directed CAR-NKT cell product demonstrated enhanced bone marrow localization and antileukemic activity in preclinical models compared to their CAR-T cell counterparts.⁵ Additionally, CAR-NKT cells have shown greater tissue residency and sustained persistence in solid tumor settings. In the neuroblastoma xenograft models, GD2-targeted CAR-NKT cells effectively localize to the tumor site compared to CAR-T cells.⁸ This is possibly due to the distinct chemokine receptor expression profile

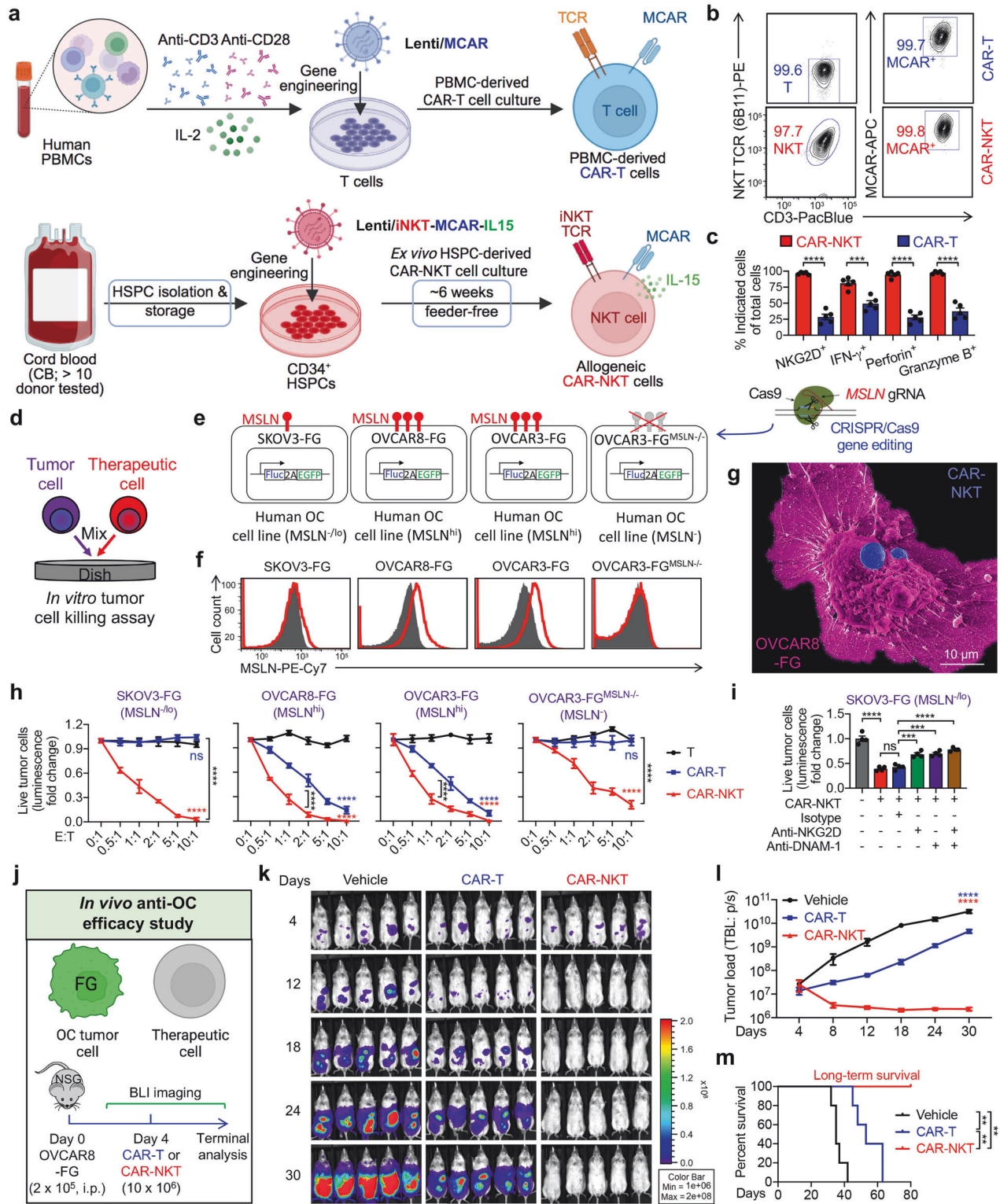
¹Department of Microbiology, Immunology & Molecular Genetics, University of California, Los Angeles, Los Angeles, CA, USA; ²Department of Bioengineering, University of California, Los Angeles, Los Angeles, CA, USA; ³Department of Biological Chemistry, David Geffen School of Medicine, University of California, Los Angeles, Los Angeles, CA, USA; ⁴Department of Molecular and Medical Pharmacology, University of California, Los Angeles, Los Angeles, CA, USA; ⁵Department of Cardiovascular Surgery, First Affiliated Hospital of Anhui Medical University, and School of Basic Medical Sciences, Anhui Medical University, Hefei, Anhui, China; ⁶Division of Cardiology, Department of Medicine, University of California, Los Angeles, Los Angeles, CA, USA; ⁷Department of Human Genetics, David Geffen School of Medicine at UCLA, Los Angeles, Los Angeles, CA, USA; ⁸Molecular Biology Institute, University of California, Los Angeles, CA, USA; ⁹Eli and Edythe Broad Center of Regenerative Medicine and Stem Cell Research, University of California, Los Angeles, Los Angeles, CA, USA; ¹⁰Jonsson Comprehensive Cancer Center, David Geffen School of Medicine, University of California Los Angeles, Los Angeles, CA, USA; ¹¹Parker Institute for Cancer Immunotherapy, University of California, Los Angeles, Los Angeles, CA, USA and ¹²Goodman-Luskin Microbiome Center, University of California, Los Angeles, Los Angeles, CA, USA

Correspondence: Yan-Ruide Li (charlie.li@ucla.edu) or Lili Yang (liliyang@ucla.edu)

These authors contributed equally: Yan-Ruide Li, Miao Li, Yuning Chen

Received: 18 August 2025 Revised: 20 December 2025 Accepted: 19 January 2026

Published online: 12 March 2026



of CAR-NKT cells, for example, higher levels of CCR5 and CXCR3 expressed in NKT cells than memory T cells.^{5,9} These findings imply that therapeutic kinetics, including expansion, trafficking, and contraction phases, may be fundamentally different between CAR-T and CAR-NKT cell therapies, yet a comprehensive head-to-head comparison has not been performed.

Checkpoint receptor signaling plays a pivotal role in modulating CAR cell activity, particularly in the immunosuppressive TME.

While immune checkpoint pathways have been extensively studied in conventional CAR-T cells (e.g., PD-1/PD-L1, Tim3/Galectin-9, LAG3/FGL-1, CTLA4/B7 molecules), far less is known about how these regulatory networks operate in CAR-NKT cells.^{10–12} As highlighted in recent literature, innate immune checkpoints such as CD96 and CD160, which are originally defined in NK cells, play a key role in modulating cytotoxic responses of NKT cells.^{13,14} CAR-NKT and CAR-T respond differently to

Fig. 1 CAR-T and CAR-NKT cells exhibit distinct anti-tumor efficacy. **a–c** Generation and characterization of human CAR-T and CAR-NKT cells. **a** Schematics showing the development of a human PBMC-derived mesothelin (MSLN)-targeting CAR-engineered conventional T (CAR-T) cells, as well as HSPC-engineered allogeneic MSLN-targeting CAR-engineered NKT (CAR-NKT) cells. PBMC peripheral blood mononuclear cell, HSPC CD34⁺ hematopoietic stem and progenitor cell, Lenti/MCAR lentiviral vector encoding an MSLN-targeting CAR, Lenti/iNKT-MCAR-IL15 lentiviral vector encoding a pair of human iNKT TCR α and β chains, an MSLN-targeting CAR, with a human soluble IL-15. **b** FACS plots showing the generation of CAR-T and CAR-NKT cells. A 6B11 monoclonal antibody was used to stain CAR. **c** FACS analyses of the expression of indicated markers of CAR-T and CAR-NKT cells ($n = 5$; n indicates different PBMC or CB donors). **d–i** Studying the in vitro tumor cell killing efficacy and mechanism of CAR-T and CAR-NKT cells. **d** Experimental design. **e** Schematics showing the four human tumor cell lines utilized in this study. All were engineered to express the firefly luciferase (Fluc) and enhanced green fluorescent protein (EGFP) dual reporters (FG). Four OC tumor cell lines were included: SKOV3-FG (MSLN^{-/0}), OVCAR8-FG (MSLN^{hi}), OVCAR3-FG (MSLN^{hi}), and OVCAR3-FG^{MSLN-/-} (OVCAR3-FG deprived of MSLN via CRISPR-Cas9 gene knock-out). **f** FACS detection of MSLN expression on the indicated tumor cells. **g** Scanning electron microscope (SEM) visualization of allogeneic CAR-NKT cells attacking OC tumor cells. A representative image is presented showing a CAR-NKT cell attacking an OVCAR8-FG cell. **h** Tumor cell killing data at 24 h ($n = 4$). Three therapeutic cells were included. **i** Studying the tumor cell killing mechanisms of CAR-NKT cells mediated by NK receptors (NKR; NKG2D and DNAM-1). Tumor cell killing data at 24 h (E:T ratio = 2:1; $n = 4$). **j–m** Studying the in vivo antitumor efficacy of CAR-T and CAR-NKT cells in an OVCAR8-FG human OC xenograft NSG mouse model. **j** Experimental design. BLI bioluminescence live animal imaging. Therapeutic cells were injected into experimental mice via intraperitoneal (i.p.) administration routes. **k** BLI images showing tumor loads in experimental mice over time. **l** Quantification of **(k)** ($n = 5$). **m** Survival curve ($n = 5$). Representative of 3 (**j–m**) and over 5 (**a–i**) experiments. Data are presented as the mean \pm SEM. ns not significant, ** $p < 0.01$, *** $p < 0.001$, **** $p < 0.0001$, by Student's t test (**c**), one-way ANOVA (**i**, **l**), two-way ANOVA (**h**), or log rank (Mantel-Cox) test adjusted for multiple comparisons (**m**)

suppressive ligands in the TME, engaging distinct inhibitory and costimulatory axes.^{4,15} These results underscore the need for tailored checkpoint blockade strategies to match the unique immunoregulatory architecture of CAR-NKT and CAR-T cells, in order to unlock their full therapeutic potential and optimize efficacy in solid tumor settings.

In this study, we employed a preclinical solid tumor model combined with spatiotemporal gene profiling to dissect the therapeutic differences between CAR-T and CAR-NKT cells. CAR-NKT cells were generated from human cord blood-derived hematopoietic stem and progenitor cells (HSPCs) using a clinically guided culture platform, providing an allogeneic, off-the-shelf modality.¹⁶ By analyzing gene expression dynamics across multiple time points and tissue compartments, we identified key distinctions in trafficking, persistence, immune modulation, and checkpoint regulation between CAR-NKT and CAR-T cells. This systems-level comparison provides mechanistic insights into the divergent antitumor properties of CAR-NKT and CAR-T cells and informs rational design of next-generation cellular immunotherapies for solid tumors.

RESULTS

Human CAR-T and CAR-NKT cells exhibit distinct anti-tumor efficacy both in vitro and in vivo

We generated two therapeutic cell products: CAR-T and CAR-NKT cells in this study (Fig. 1a). CAR-T cells were derived from healthy donor peripheral blood mononuclear cells (PBMCs) and transduced with a lentiviral vector encoding a mesothelin (MSLN)-targeting CAR, enabling them to recognize and kill MSLN-expressing solid tumor cells (Fig. 1a). The CAR-T cell manufacturing process followed established clinical-grade protocols, consistently yielding a balanced CD4/CD8 ratio across all healthy donor-derived PBMCs (Supplementary Fig. 1a, b). CAR-NKT cells were generated from HSPCs using a clinically guided differentiation protocol previously applied in blood cancer settings.^{5,16} In this study, we adapted this method to generate CAR-NKT cells targeting MSLN-positive solid tumors (Fig. 1a). These cells were further engineered to express human soluble IL-15 (Fig. 1a), a modification shown in both preclinical and clinical studies to enhance CAR-NKT cell persistence and antitumor efficacy.^{16–18}

Both cell products demonstrated high purity: over 97% of CAR-NKT cells were NKT TCR⁺CD3⁺CAR⁺, and over 99% of CAR-T cells were NKT TCR⁻CD3⁺CAR⁺ (Fig. 1b). In CAR-NKT cells, the NKT TCR and CAR were co-expressed from the same lentiviral construct, ensuring uniform CAR expression after HSPC differentiation and TCR positive selection.^{19,20} However, due to inherent limitations in

transduction efficiency, CAR-T cells exhibited ~50–70% CAR expression and required additional purification (e.g., FACS sorting) to enrich for CAR⁺ cells. Phenotypic analysis revealed that CAR-NKT cells expressed significantly higher levels of NK receptors (NKR; e.g., NKG2D), proinflammatory cytokines (e.g., IFN- γ), and cytotoxic mediators (e.g., Perforin and Granzyme B) compared to CAR-T cells, suggesting a more robust cytotoxic potential (Fig. 1c).

We then assessed the cytotoxicity of CAR-T and CAR-NKT cells using four ovarian cancer (OC) cell lines: SKOV3, OVCAR8, OVCAR3, and OVCAR3-MSLN^{-/-} (CRISPR-Cas9 knockout of MSLN) (Fig. 1d–f). These lines expressed varying levels of MSLN, allowing us to evaluate both CAR-dependent and CAR-independent killing mechanisms (Fig. 1f). All tumor cells were engineered to co-express firefly luciferase and enhanced green fluorescence protein (EGFP) dual reporters (FG), enabling visualization via fluorescence and bioluminescence (Fig. 1e).

Scanning electron microscopy (SEM) confirmed direct contact and cytolytic morphology of CAR-NKT cells engaging OVCAR8-FG cells (Fig. 1g). In vitro killing assays demonstrated that unmodified T cells failed to kill any tumor cell lines (Fig. 1h). CAR-T cells efficiently killed MSLN⁺ tumor cells but had no effect on MSLN⁻ targets, consistent with CAR-restricted activity (Fig. 1h). In contrast, CAR-NKT cells exhibited potent killing of all tumor lines, including OVCAR3-MSLN^{-/-}, though the killing was more effective against MSLN⁺ cells (Fig. 1h). These data indicate that CAR-NKT cells utilize both CAR-dependent and CAR-independent cytotoxic mechanisms. Furthermore, blocking assays confirmed that inhibition of NKR (i.e., NKG2D and DNAM-1) reduced CAR-NKT cytotoxicity, further supporting their role in CAR-NKT cell-mediated tumor recognition (Fig. 1i).

To dissect the contributions of CAR and IL-15 to the phenotype and functionality of CAR-NKT cells, we generated two additional therapeutic cell types from CB HSPCs: non-CAR-engineered NKT cells and CAR-NKT cells lacking IL-15 engineering, denoted as NKT and CAR-NKT (no IL-15) cells, respectively (Supplementary Fig. 1c, d). All three NKT-derived products exhibited a similar phenotype, characterized by high expression of NKR (e.g., NKG2D) and robust effector molecule production (e.g., IFN- γ , Perforin, and Granzyme B) (Supplementary Fig. 1e). In a 24-hour tumor cell killing assay, all three NKT products efficiently lysed tumor cells regardless of MSLN expression, consistent with intrinsic NKR-mediated cytotoxicity (Supplementary Fig. 1f, g). However, against MSLN⁺ tumor cells such as OVCAR3-FG and OVCAR8-FG, both CAR-NKT and CAR-NKT (no IL-15) cells demonstrated superior cytotoxicity compared with NKT cells, indicating additional CAR-mediated killing (Supplementary Fig. 1f, g). Within this 24-hour short-term assay, IL-15 provided only limited

enhancement of CAR-NKT cytotoxicity. We next performed a long-term in vitro tumor cell killing assay, in which tumor cells were reintroduced every 2 days, to assess sustained antitumor activity (Supplementary Fig. 1h). Under these conditions, IL-15-engineered CAR-NKT cells achieved the most durable tumor control, maintaining potent cytotoxicity through 10 rounds of tumor rechallenge (Supplementary Fig. 1i). These findings indicate that IL-15 plays a critical role in supporting the long-term persistence and antitumor capacity of CAR-NKT cells.

We next evaluated the therapeutic potential of CAR-T and CAR-NKT cells in an intraperitoneal (i.p.) xenograft model of human ovarian cancer using OVCAR8-FG cells (Fig. 1j). Tumor-bearing mice received localized i.p. injections of either CAR-T or CAR-NKT cells, and tumor progression was monitored via bioluminescent imaging (BLI). CAR-T cell treatment delayed tumor growth but failed to achieve complete tumor elimination, and all treated mice eventually succumbed to disease (Fig. 1k–m and Supplementary Fig. 2a). In contrast, CAR-NKT cells achieved complete tumor clearance in all treated mice, resulting in long-term survival (Fig. 1k–m and Supplementary Fig. 2a). These results demonstrate the superior in vivo antitumor efficacy of CAR-NKT cells in this OC xenograft mouse model.

Interestingly, we noticed that compared to conventional CAR-T cells, HSPC-derived CAR-NKT cells exhibited markedly lower levels of HLA-I molecules and nearly undetectable HLA-II molecules (Supplementary Fig. 2b, c). These findings were consistent across in vitro generated cell products and in vivo peritoneal fluid-isolated tumor-infiltrating cells (Supplementary Fig. 2b–d). Together, these results suggest that allogeneic CAR-NKT cells possess hypoinmunogenic properties, which may reduce susceptibility to host T cell-mediated alloreactivity.^{16,21,22} Nonetheless, low levels of HLA-I expression remain detectable, and further genetic engineering of HLA molecules (e.g., CRISPR knockouts of *B2M* and *CIITA* genes) may be required to achieve fully universal, off-the-shelf products.^{6,22,23}

In summary, we developed and characterized two distinct CAR-engineered immune cell therapies targeting MSLN-expressing solid tumors. CAR-NKT cells, generated via HSPC engineering and further enhanced with IL-15, displayed reduced HLA expression, superior cytotoxicity, broader target recognition, and more effective in vivo tumor control compared to conventional CAR-T cells. Importantly, HSPC-derived CAR-NKT cells are truly off-the-shelf, with high purity, consistent 100% CAR expression, and scalable production. By contrast, conventional CAR-T cells exhibit variable transduction efficiency, are autologous, and cannot be readily delivered to multiple patients. Although in clinical practice CAR-T cells generally do not require additional purification, and this step does not significantly affect their antitumor efficacy (Supplementary Fig. 2e, f), they remain limited by scalability and accessibility.^{24–26} Therefore, HSPC-derived CAR-NKT cells represent a promising and balanced platform for the development of universal, scalable, and clinically accessible CAR-based immunotherapies.

CAR-T and CAR-NKT cells exhibit distinct in vivo pharmacokinetics and pharmacodynamics (PK/PD) during antitumor response. To investigate the in vivo PK/PD of CAR-T and CAR-NKT cells, we engineered both cell types to co-express FG, enabling real-time, non-invasive tracking via BLI (Fig. 2a). The in vivo model mirrored the previously described OC efficacy study, except that in this experiment, the tumor cells were not FG-labeled, but only the therapeutic cells carried the FG reporter to monitor their biodistribution and persistence over time (Figs. 1j and 2a).

CAR-T and CAR-NKT cells exhibited markedly different in vivo behaviors. Following i.p. injection, CAR-T cells initially localized within the peritoneal cavity (Fig. 2b–e). However, by approximately day 30 post-injection, these cells began to disseminate systemically, with increasing signals detected in secondary

lymphoid organs and peripheral tissues such as the lymph nodes, spleen, and lungs (Fig. 2b–e). A dramatic expansion of CAR-T cells was observed by day 50, suggesting uncontrolled proliferation (Fig. 2b–e). This systemic spread and expansion were associated with xenogeneic graft-versus-host disease (xeno-GvHD), ultimately leading to mortality in CAR-T cell-treated experimental mice.

In contrast, CAR-NKT cells demonstrated a more controlled and localized expansion profile. These cells expanded gradually over the first 40 days post-injection, followed by a steady decline and long-term persistence detectable beyond 100 days (Fig. 2b–e). Importantly, CAR-NKT cells remained largely confined to the peritoneal cavity, with minimal dissemination to peripheral tissues (Fig. 2b–e). This strict localization likely contributed to their reduced systemic toxicity and absence of GvHD-related mortality. We observed a rapid expansion followed by contraction of CAR-NKT cells in vivo, a PK/PD pattern consistent with our previous studies using BCMA-targeting CAR-NKT cells in human multiple myeloma xenograft models.¹⁶ The initial expansion is driven by antigen-specific stimulation through the tumor-associated antigen MSLN, coupled with IL-15-mediated support, which promotes robust proliferation of CAR-NKT cells (Fig. 2b, c). Once the tumor cells are largely eliminated and antigenic stimulation diminishes, CAR-NKT cells gradually contract, reflecting a self-limiting response (Figs. 1j–m and 2b, c). This controlled expansion and contraction not only mirror physiological immune kinetics but also underscore the safety profile of CAR-NKT cells, as their proliferation is antigen-dependent and does not result in uncontrolled growth or tumorigenesis.

Flow cytometric analysis confirmed these imaging findings. CAR-T cells were initially detected in the peritoneal fluid but later became abundant in the blood, reflecting systemic migration (Fig. 2f, g). Conversely, CAR-NKT cells were largely restricted to the peritoneal environment, with minimal presence in circulation (Fig. 2f, g).

In addition, we measured serum IL-15 levels in mice infused with CAR-NKT cells on days 20, 40, 75, and 115. The cytokine levels positively correlated with CAR-NKT cell expansion in vivo, suggesting that the elevated IL-15 was produced by the CAR-NKT cells themselves and contributed to their sustained persistence and proliferation (Supplementary Fig. 2g).

These results underscore fundamental differences in the pharmacokinetics, tissue trafficking, and safety profiles between CAR-T and CAR-NKT cells. CAR-T cells exhibit robust expansion and systemic distribution, which, while potentially enhancing anti-tumor responses, may also increase the risk of toxicity, including xeno-GvHD in preclinical models (Supplementary Fig. 2h). In contrast, CAR-NKT cells exhibit tissue-restricted persistence and controlled expansion, contributing to durable antitumor activity with a favorable safety profile models (Supplementary Fig. 2h).²⁷ Together, these findings highlight the translational potential of CAR-NKT cells as a safer and more targeted cellular immunotherapy for solid tumors. Their unique pharmacologic behavior suggests a reduced risk of systemic toxicity while maintaining effective local tumor control, making them particularly well-suited for compartmentalized tumors such as those found in the peritoneal cavity.

CAR-NKT cells demonstrate a high tumor retention capacity driven by their distinct chemokine receptor expression pattern. We further investigated the molecular mechanisms underlying the superior tumor retention capacity of CAR-NKT cells by comparing their chemokine receptor expression patterns with those of conventional CAR-T cells. In tumor-infiltrating cells isolated in vivo, CAR-NKT cells exhibited almost no expression of S1PR1 but markedly higher levels of CD69 compared to CAR-T cells (Supplementary Fig. 3a). This S1PR1^{low}CD69^{high} phenotype is known to promote tissue residency and reduce recirculation through the blood, thereby supporting enhanced tumor retention.^{21,28}

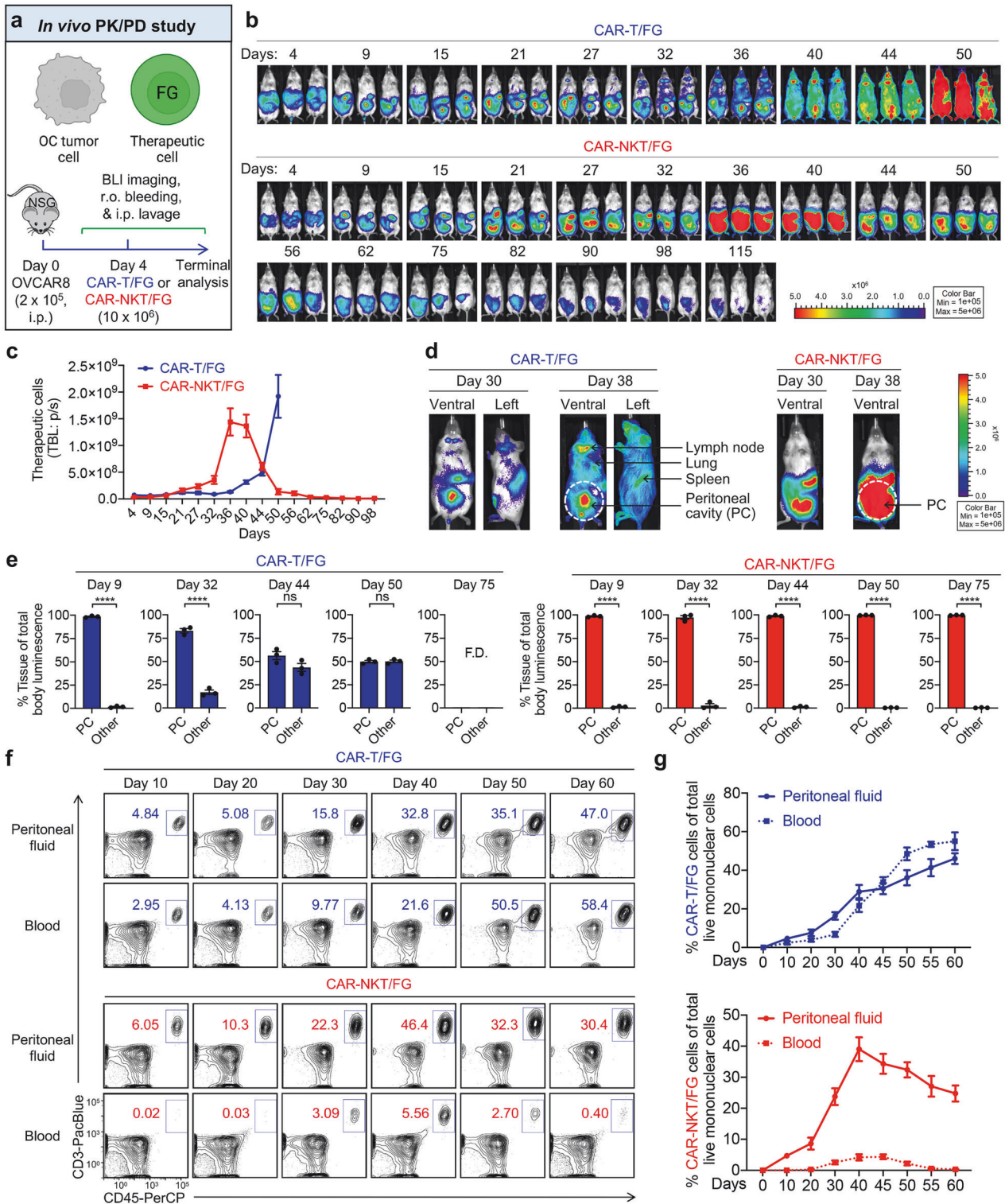
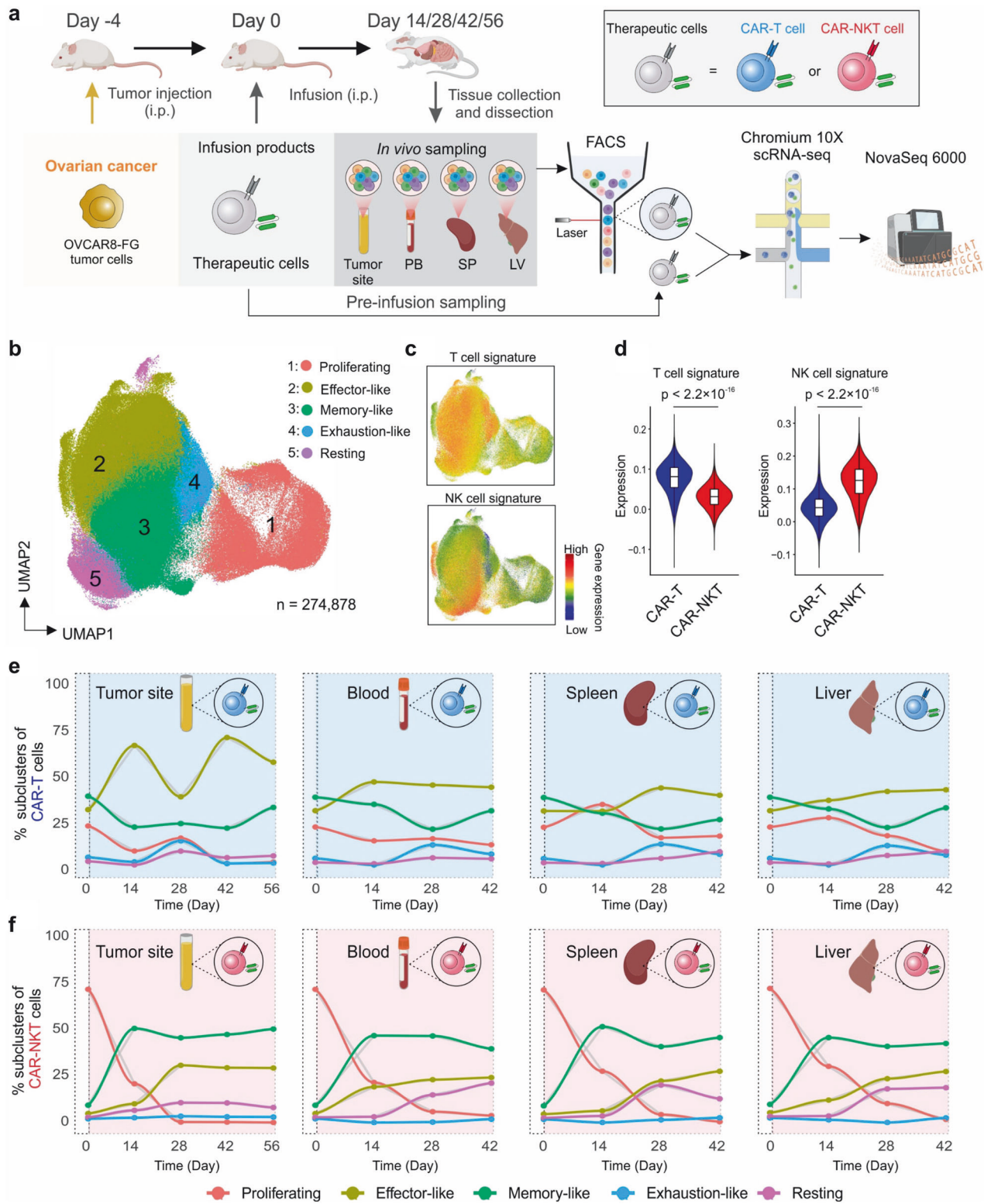


Fig. 2 CAR-T and CAR-NKT cells exhibit distinct in vivo pharmacokinetics and pharmacodynamics (PK/PD) during antitumor response. **a** Experimental design to study the in vivo PK/PD in an OVCAR8 human ovarian cancer xenograft NSG mouse model. Note the therapeutic cells, but not the OVCAR8 tumor cells, were labeled with the FG. **b** BLI images showing the presence of therapeutic cells in experimental mice over time. **c** Quantification of (b) ($n = 3$). **d** Representative BLI images showing the biodistribution of therapeutic cells in the indicated experimental mice. **e** Quantification of the tissue distribution of therapeutic cells ($n = 3$). F.D. found dead. **f** FACS detection of CAR-T and CAR-NKT cells in the peritoneal fluid and blood of the experimental mice over time. **g** Quantification of (f) ($n = 5$). Representative of 2 experiments. Data are presented as the mean \pm SEM. ns not significant, **** $p < 0.0001$, by Student's t test (e)



In addition, we analyzed a panel of tissue- and inflammation-associated chemokine receptors, including CCR1, CCR5, CXCR3, and CXCR6. CAR-NKT cells expressed substantially higher levels of these receptors than CAR-T cells, indicating an intrinsically superior capacity for tumor homing and infiltration (Supplementary Fig. 3a).^{9,29} Conversely, analysis of CD62L and CCR7, which are markers associated with lymph node homing, revealed that CAR-NKT cells expressed

markedly lower levels of these molecules, suggesting a reduced propensity for lymphoid tissue trafficking and a preferential localization within tumor sites (Supplementary Fig. 3a).³⁰

This distinct chemokine receptor expression pattern was further validated by scRNA-seq analysis, which confirmed that CAR-NKT cells maintain a transcriptional program consistent with tissue-resident, inflammatory effector cells (Supplementary Fig. 3b).

Fig. 3 Spatiotemporal gene profiling reveals distinct cluster dynamics between CAR-T and CAR-NKT cells. **a** Schematic of the experimental design to study the gene profiling of conventional CAR-T cells and CAR-NKT using single-cell RNA sequencing (scRNA-seq). Samples from tissues including the peritoneal cavity (tumor site), peripheral blood (PB), spleen (SP) and liver (LV) were collected at five timepoints: day 0 (pre-infusion), day 14, day 28, day 42 and day 56. Therapeutic cells were subjected to FACS sorting. Sorted CD45⁺ and CD3⁺ live cells were analyzed using droplet-based 10x Genomics Chromium scRNA-seq approach. **b** UMAP plot showing the formation of five major cell clusters from integrated datasets of CAR-T and CAR-NKT cells. The combined total 274,878 cells concatenated are included. Each dot represents a single cell and is colored according to its cell cluster assignment. **c** UMAP plots showing the expression the indicated gene signatures. Each dot represents a single cell and is colored according the combined expression of the indicated gene signatures. **d** Violin plots showing the expression distribution of T cell and NK cell signatures of genes in indicated cell types. Line plots showing the percentage of CAR-T (**e**) and CAR-NKT cells (**f**) in each cluster across specified tissues over time. Representative of 1 experiment. Cells isolated from 5-10 mice of each experimental group were combined for analyses. *P* values of violin plots were determined by Kruskal–Wallis test for the overall comparison and Dunn’s test for post hoc pairwise comparisons between groups. In the violin plots, box and whisker plots exhibit the minimum, lower quartile, median, upper quartile and maximum expression levels of each type of cells

Collectively, these results reveal that CAR-NKT cells possess a unique chemokine receptor signature that underlies their superior tumor retention capacity and sustained intratumoral persistence, contributing to their enhanced antitumor efficacy (Supplementary Fig. 3c).

CAR-NKT cells exhibit potent NK-like tumor cytotoxicity and a favorable safety profile compared with IL-15-boosted CAR-T cells. HSPC-derived CAR-NKT cells were engineered to express IL-15, which has been shown to enhance the *in vivo* persistence and functionality of both CAR-T and CAR-NKT cells.³¹ To directly compare the effect of IL-15, we similarly engineered conventional CAR-T cells to express human soluble IL-15 and performed side-by-side comparisons of tumor-targeting capacity between IL-15-boosted CAR-T and CAR-NKT cells (Supplementary Fig. 4a–f).

In an *in vitro* tumor cell killing assay using four OC cell lines, CAR-NKT cells exhibited robust cytotoxicity against both MSLN^{hi} (OVCAR8-FG and OVCAR3-FG) and MSLN^{lo} (SKOV3-FG and OVCAR3-FG^{MSLN^{-/-}}) targets, outperforming IL-15-boosted CAR-T cells (Supplementary Fig. 4g). Notably, despite IL-15 engineering, CAR-T cells showed minimal improvement in cytotoxicity compared to conventional CAR-T cells within the short-term assay window (Fig. 1h and Supplementary Fig. 4h). Therefore, CAR-NKT cells retained superior antitumor activity through multiple tumor-targeting mechanisms, including both CAR- and NKR-mediated cytotoxicity, consistent with their high NKR expression and effector molecule production (Supplementary Fig. 4f).

We then evaluated the *in vivo* antitumor activity in the OVCAR8-FG human OC xenograft mouse model (Supplementary Fig. 4i). IL-15-boosted CAR-T cells demonstrated enhanced antitumor efficacy, with all mice achieving tumor elimination by day 30 (Supplementary Fig. 4j, k). However, all experimental mice succumbed to treatment-associated toxicity. Blood and tissue analyses revealed massive expansion of IL-15-boosted CAR-T cells, with these cells comprising over 50% of mononuclear cells in multiple organs, leading to severe body weight loss, elevated clinical GvHD scores, and ultimately death (Supplementary Fig. 4l–p). Additionally, using a previously established xenograft model in which human CAR-T cells interact with mouse peritoneal macrophages to induce a cytokine release syndrome (CRS)-like response (Supplementary Fig. 4q),³² we observed that IL-15-boosted CAR-T cells triggered a pronounced CRS phenotype. Specifically, treated mice exhibited rapid body weight loss and mortality (Supplementary Fig. 4r, s). ELISA analyses further revealed markedly elevated serum levels of CRS-associated biomarkers, including mouse IL-6 and SAA-3 (Supplementary Fig. 4t, u). These findings are consistent with a recent clinical trial using IL-15-enhanced GPC3-targeting CAR-T cells in HCC patients, which reported IL-15-mediated severe CRS.³³ Thus, although IL-15 enhances CAR-T antitumor activity, its associated toxicity presents a significant safety concern.

Importantly, no IL-15-related toxicity was observed in CAR-NKT cells in our preclinical models or in a recent clinical trial of CAR-

NKT cells in pediatric neuroblastoma patients (Supplementary Fig. 4i–u).¹⁸ This suggests that IL-15 confers a more favorable safety profile in CAR-NKT cells, enabling improved *in vivo* persistence and antitumor efficacy without inducing severe systemic toxicity, highlighting CAR-NKT cells as a potentially safer platform for IL-15-based enhancements.

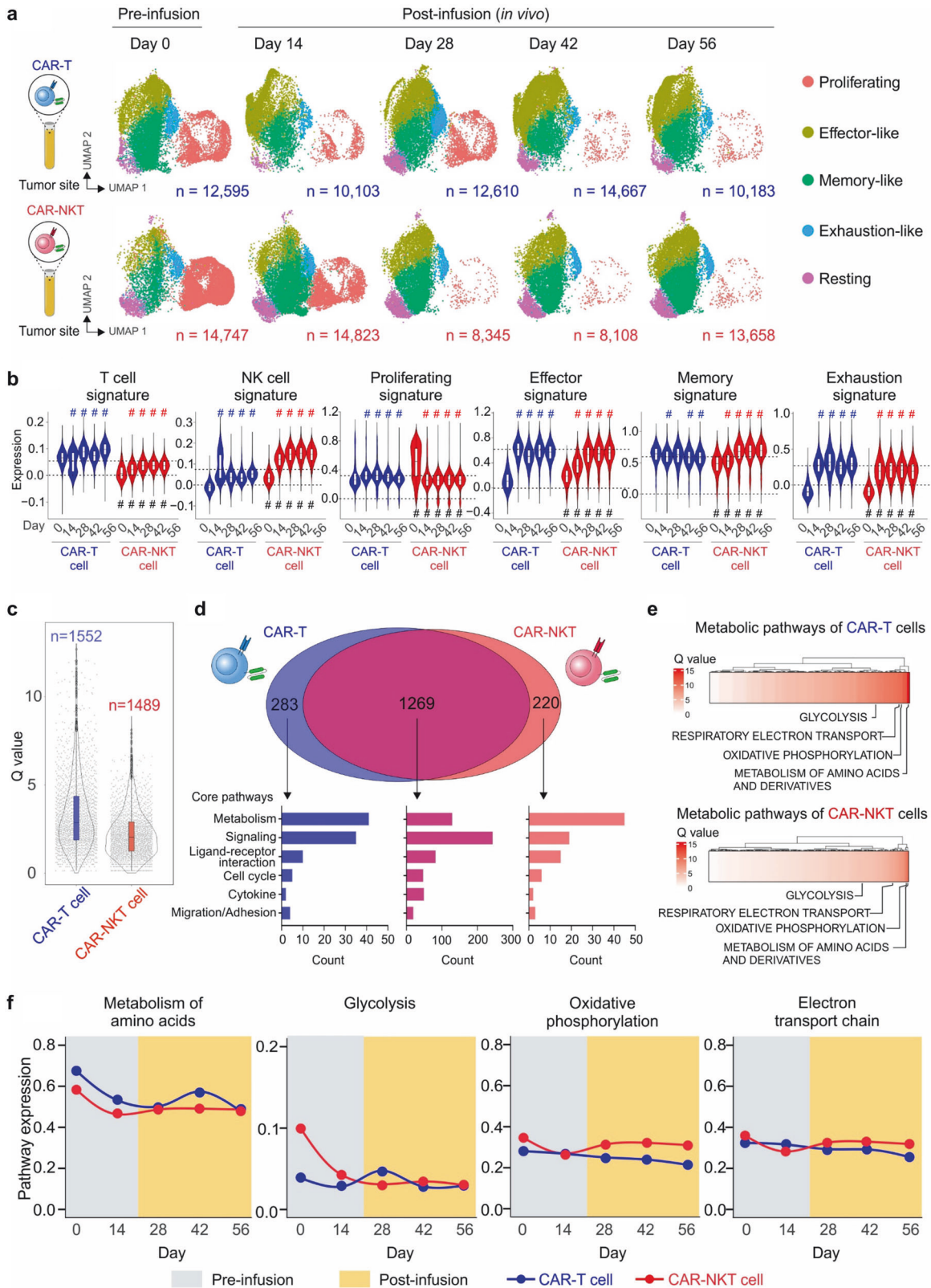
Spatiotemporal gene profiling reveals distinct cluster dynamics between CAR-T and CAR-NKT cells

To elucidate the genomic and molecular programs underlying the *in vivo* antitumor functions of CAR-T and CAR-NKT cells, we performed single-cell RNA sequencing (scRNA-seq) using cells isolated from the OVCAR8-FG xenograft mouse model (Fig. 3a). Therapeutic cells were collected at five time points—Day 0 (pre-infusion baseline), and Days 14, 28, 42, and 56 post-infusion—from multiple tissue compartments, including tumor sites (peritoneal fluid), blood, spleen, and liver. This design enabled a comprehensive, longitudinal analysis of the transcriptional and phenotypic states of CAR-T and CAR-NKT cells during tumor engagement *in vivo* (Fig. 3a).

Uniform manifold approximation and projection (UMAP) analysis of integrated scRNA-seq data revealed five major cell clusters (Fig. 3b). Based on gene signature profiling and gene set enrichment analysis (GSEA), these clusters were annotated as: proliferating (Cluster 1), effector-like (Cluster 2), memory-like (Cluster 3), exhaustion-like (Cluster 4), and resting cells (Cluster 5) (Fig. 3b and Supplementary Fig. 5).¹⁶ Violin plots of canonical T cell and NK cell gene expression showed clear lineage distinctions: CAR-T cells exhibited higher T cell-associated gene signatures, while CAR-NKT cells expressed elevated NK-like signatures (Fig. 3c, d).

Notably, CAR-T and CAR-NKT cells exhibited distinct cluster dynamics over time and across tissue compartments (Fig. 3e, f). In CAR-T cells, the effector-like population displayed fluctuating frequencies within the tumor site, while remaining relatively stable in other tissues (Fig. 3e, f). By contrast, CAR-NKT cells showed a consistent decrease in the proliferating cluster after infusion, accompanied by stable and elevated levels of effector-like and memory-like populations across all tissues (Fig. 3e, f). Importantly, the memory-like population predominated among CAR-NKT cells throughout the observation period. Moreover, CAR-NKT cells maintained a low frequency of exhaustion-like cells across tissues and time points, in contrast to CAR-T cells, which exhibited increased exhaustion-like features, particularly on day 28 (Fig. 3e, f). This time point corresponds to prolonged tumor exposure and precedes the rapid expansion and systemic migration of CAR-T cells from the peritoneal cavity, likely triggered by xeno-GvHD (Fig. 2). These findings suggest that CAR-T cell exhaustion in xenograft models is influenced by multiple factors, including sustained tumor antigen stimulation and xeno-GvHD. This also underscores the importance of carefully evaluating CAR-T cell PK/PD in both preclinical models and clinical settings.

Collectively, these findings demonstrate that CAR-T and CAR-NKT cells adopt distinct spatiotemporal transcriptional



programs during solid tumor engagement. CAR-NKT cells maintain durable effector and memory phenotypes with minimal exhaustion, suggesting superior functional persistence and therapeutic potential in the immunosuppressive TME of solid tumors.

Intratumoral time-course gene profiling reveals different metabolic dynamics between CAR-T and CAR-NKT cells. To investigate the intratumoral behavior and metabolic dynamics of CAR-T and CAR-NKT cells, we performed single-cell transcriptomic analysis of tumor-infiltrating cells collected at multiple time

Fig. 4 Intratumoral time-course gene profiling reveals different metabolic dynamics between CAR-T and CAR-NKT cells. **a** UMAP plots of CAR-T and CAR-NKT cells collected at indicated time points in tumor site. Each dot represents a single cell and is colored according to its cell cluster assignment. **b** Violin plots showing the expression distribution of indicated gene signature in CAR-T and CAR-NKT cells collected at each time point. *P* values for the violin plots were calculated using two-tailed Wilcoxon rank-sum tests. # labels indicate statistical significance. In each violin plot, the # above the violin denotes significance compared with the corresponding cells at Day 0, while the # below the violin denotes significance compared with the other therapeutic cell type at the same day. **c–f** Single-cell pathway analysis (SCPA) of CAR-T and CAR-NKT cells in tumor site across time. **c** Violin plots showing the distribution of all pathways analyzed (1,790 in totals). *n* indicates the number of significant pathways (*Q* value > 0 and *p* value < 0.05). **d** Venn diagram illustrating the number of shared and unique pathways between CAR-T and CAR-NKT cells. The frequencies of the indicated core pathways in each category are quantified and showed in bar plots. **e** Heatmaps showing the enrichment of the indicated metabolic pathways in CAR-T and CAR-NKT cells. **f** Line plots showing the expression levels of the indicated metabolic pathways in CAR-T and CAR-NKT cells over time

points: pre-infusion (Day 0) and post-infusion (Days 14, 28, 42, and 56) (Fig. 4a). UMAP visualization revealed distinct clustering trajectories for CAR-T and CAR-NKT cells over time, with dynamic changes in phenotypic states (Fig. 4a, b and Supplementary Fig. 6a). Compared to pre-infusion samples, CAR-T cells in vivo exhibited increased expression of T cell, NK cell, proliferative, effector, and exhaustion signatures (Fig. 4b). Notably, the acquisition of NK-like features by CAR-T cells in vivo is consistent with an exhaustion-associated transcriptional program described in previous studies.³⁴ Across all four in vivo time points, CAR-T cells maintained relatively stable phenotypes, with a slight decline in proliferative signatures (Fig. 4b and Supplementary Fig. 6a).

In contrast, CAR-NKT cells displayed progressive enhancement of T cell, NK cell, effector, memory, and exhaustion signatures, while their proliferative signature declined over time (Fig. 4b and Supplementary Fig. 6a). The gradual increase in NK-, effector-, and memory-like features suggests that CAR-NKT cells undergo a maturation process within the TME, developing sustained effector and memory phenotypes with reduced reliance on active proliferation. When directly comparing CAR-T and CAR-NKT cells in vivo, CAR-NKT cells exhibited lower T cell signature, higher NK signature, comparable effector function, elevated memory features, and reduced exhaustion (Fig. 4b and Supplementary Fig. 6a). These findings indicate that CAR-NKT cells maintain a more balanced activation state, favoring long-term persistence and reduced exhaustion within the TME.

The scRNA-seq transcriptomic analyses were further validated using flow cytometry and additional functional assays. For example, flow cytometric detection of the proliferation marker Ki-67 in CAR-T and CAR-NKT cells, both from in vitro cultures and in vivo isolates, revealed that CAR-NKT cells exhibited higher Ki-67 expression than CAR-T cells in vitro (Supplementary Fig. 6b, c). In contrast, in vivo isolated CAR-T and CAR-NKT cells displayed comparable Ki-67 levels, with CAR-NKT cells remaining slightly higher (Supplementary Fig. 6b, c). These findings support our scRNA-seq analysis and demonstrate that CAR-NKT cells possess a more proliferative phenotype in vitro, which is sustained in vivo.

To further explore the functional implications of these differences, we performed single-cell pathway analysis (SCPA) on 1,790 biological pathways. CAR-T cells showed broader pathway enrichment overall, as evidenced by a wider distribution of pathway scores (Fig. 4c). Venn diagram analysis identified 1,269 pathways shared by both cell types, with 283 uniquely enriched in CAR-T cells and 220 in CAR-NKT cells (Fig. 4d). These unique pathways were primarily related to metabolic activity and T/NK cell signaling.

Focused metabolic pathway enrichment analysis revealed differences in glycolysis, oxidative phosphorylation, electron transport chain activity, and amino acid metabolism between CAR-T and CAR-NKT cells (Fig. 4e, f and Supplementary Fig. 7). Line plot analyses showed that CAR-NKT cells maintained sustained oxidative phosphorylation and electron transport activity over time, indicating preserved metabolic fitness and flexibility (Fig. 4f and Supplementary Fig. 7). CAR-T cells exhibited fluctuating amino acid metabolism, consistent with dynamic changes in their

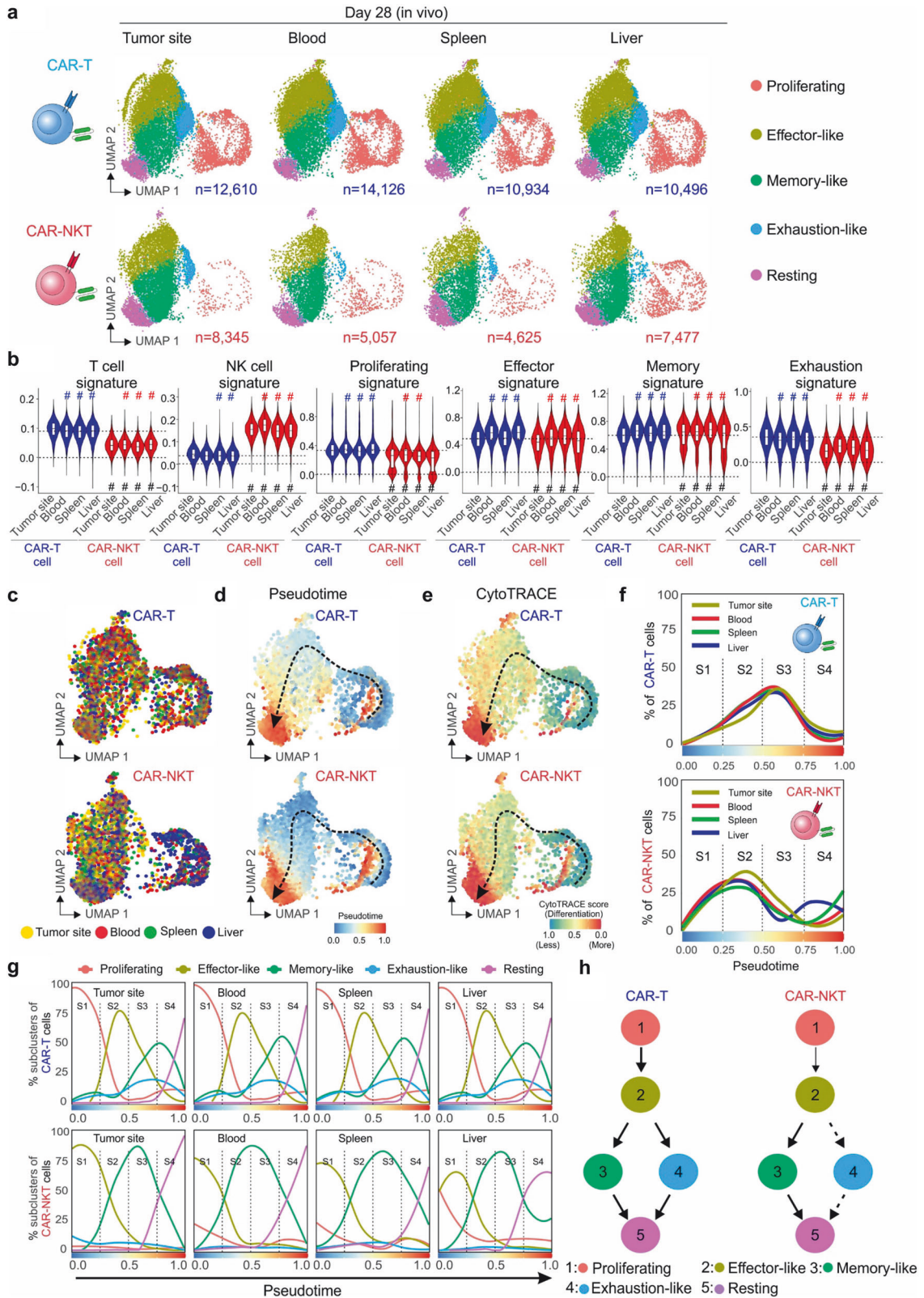
effector, memory, and exhausted states, whereas CAR-NKT cells maintained stable amino acid metabolism across all in vivo time points (Fig. 4b, f and Supplementary Fig. 7).

To validate the RNA-seq analyses, we further performed metabolite profiling of CAR-T and CAR-NKT cells using liquid chromatography–mass spectrometry (LC-MS). In vitro cultured CAR-T and CAR-NKT cells derived from multiple donors were compared. Metabolomic profiling revealed distinct differences between the two cell types. CAR-NKT cells exhibited higher activity in several metabolites, including fructose-6-phosphate, taurine, AMP/ADP, and N-acetylglucosamine-phosphate (Supplementary Fig. 8). Notably, CAR-NKT cells showed a significant enrichment of lipid metabolism-related metabolites, such as glycerol-3-phosphate, phosphocholine, glycerophosphocholine, phosphorylethanolamine, and oleic acid (Supplementary Fig. 8). These findings are consistent with the unique biology of NKT cells, which utilize their invariant TCR to recognize glycolipid antigens presented by CD1d molecules.^{35,36} It is also important to note that the metabolomic analyses were performed on in vitro-activated cells, whereas the scRNA-seq data were obtained from cells directly isolated in vivo. This difference in experimental context may contribute to variations in metabolic signatures, which could in turn influence the distinct functional behaviors of CAR-T and CAR-NKT cells upon infusion into tumor-bearing hosts.

Tissue-wide gene profiling reveals slower cross-tissue equilibrium and less divergent progression of CAR-NKT cells compared to CAR-T cells

To examine the tissue-wide distribution and progression of CAR-T and CAR-NKT cells, we performed single-cell transcriptomic profiling of cells collected on Day 28 post-infusion from the tumor site, blood, spleen, and liver. UMAP visualization revealed distinct clustering of CAR-T and CAR-NKT cells across tissues, with cells distributed among five functional states: proliferating, effector-like, memory-like, exhaustion-like, and resting (Fig. 5a). Notably, the tumor site contained a higher proportion of exhaustion-like CAR-T cells, while CAR-NKT cells in the tumor site predominantly retained effector-like and memory-like phenotypes (Fig. 5a).

Violin plots of tissue-specific gene signature expression further highlighted the differences between CAR-T and CAR-NKT cells (Fig. 5b and Supplementary Fig. 9). Across all tissues, CAR-NKT cells exhibited lower expression of T cell signatures but higher expression of NK cell signatures compared to CAR-T cells, reflecting their distinct lineage characteristics (Fig. 5b and Supplementary Fig. 9). Regarding the proliferating gene signature, CAR-NKT cells displayed consistently lower expression levels than CAR-T cells across all tissues, with neither cell type showing significant variation among tissues. In tumor sites, CAR-T cells demonstrated markedly reduced effector and memory signatures, but elevated exhaustion signatures compared to their counterparts in peripheral tissues, suggesting that tumor-infiltrating CAR-T cells undergo functional exhaustion and diminished effector differentiation (Fig. 5b and Supplementary Fig. 9). In contrast, CAR-



NKT cells within tumors exhibited slightly lower effector but consistently high memory and low exhaustion signatures, indicating a more uniform and less terminally differentiated phenotype across tissues (Fig. 5b and Supplementary Fig. 9). When directly compared, CAR-NKT cells showed comparable

effector features, higher memory signatures, and significantly lower exhaustion features than CAR-T cells, representing an effector/memory-enriched, exhaustion-low profile likely contributing to their superior in vivo antitumor activity (Fig. 5b and Supplementary Fig. 9).

Fig. 5 Tissue-wide gene profiling reveals slower cross-tissue equilibrium and less divergent progression of CAR-NKT cells compared to CAR-T cells collected on Day 28 of post-infusion. **a** UMAP plots of CAR-T and CAR-NKT cells collected at indicated tissue. Each dot represents a single cell and is colored according to its cell cluster assignment. **b** Violin plots showing the expression distribution of indicated gene signature in CAR-T and CAR-NKT cells collected from each tissue. *P* values for the violin plots were calculated using two-tailed Wilcoxon rank-sum tests. # labels indicate statistical significance. In each violin plot, the # above the violin denotes significance compared with the corresponding cells in tumor sites, while the # below the violin denotes significance compared with the other therapeutic cell type within the same tissue. **c** UMAP plots showing the single-cell tissue distributions for CAR-T and CAR-NKT cells. Each dot represents a single cell and is colored according to its tissue assignment. **d** Pseudotime directionality projection on UMAP plots. Each dot represents a single cell and is colored according to its assigned pseudotime value. Dotted lines indicate the pseudotime trajectories. **e** CytoTRACE scores projection on UMAP plots. Each dot represents a single cell and is colored according to its assigned CytoTRACE score. Dotted lines indicate the differentiation trajectories. **f** Line plots showing the percentage of CAR-T and CAR-NKT cells across specified tissues over the pseudotime trajectory. **g** Line plots showing the percentage of sub-clusters in CAR-T and CAR-NKT cells across specified tissues over the pseudotime trajectory. **h** Diagrams summarizing the progression of cell sub-clusters. The transitions between cell clusters are symbolized using connecting arrows

To investigate tissue-specific dynamics, we projected single-cell distributions across tissues onto UMAP plots, coloring cells by their tissue of origin (Fig. 5c). CAR-T cells exhibited substantial inter-tissue divergence, while CAR-NKT cells showed a higher proportion of tumor-site cells, highlighting their superior tumor infiltration capability (Fig. 5c). Pseudotime analysis further demonstrated divergent developmental trajectories between CAR-T and CAR-NKT cells (Fig. 5d). The pseudotime trajectories of CAR-T cells were characterized by a rapid transition through proliferative and effector-like states, while CAR-NKT cells progressed at a more gradual pace through these functional states, with a prolonged period in memory-like states (Fig. 5d). We also used CytoTRACE to explore the differentiation potential of CAR-T and CAR-NKT cells (Fig. 5e). CAR-T cells exhibited a pronounced decrease in differentiation potential along the pseudotime trajectory, corresponding with rapid progression towards effector and exhaustion states. On the other hand, CAR-NKT cells maintained a relatively higher differentiation potential throughout the trajectory, suggesting a more balanced differentiation state across tissues (Fig. 5e).

The temporal dynamics of CAR-T and CAR-NKT cells along the pseudotime trajectory suggest that CAR-T cells undergo distinct shifts in cell states across tissues, transitioning more readily between proliferating, effector-like, and exhaustion-like states (Fig. 5f). For CAR-T cells, there is a marked peak in the tumor site and spleen tissues during S2 and S3 stages, indicating a higher proportion of cells in these tissues at intermediate pseudotime points (Fig. 5f). In contrast, CAR-NKT cells displayed a more even distribution across tissues, with notable peaks during the S2 stage and another significant accumulation in the liver during the S3 and S4 stages (Fig. 5f). This pattern suggests that CAR-NKT cells preferentially localize to the liver at later pseudotime stages. These findings underscore the distinct tissue-specific dynamics and migratory behaviors of CAR-T and CAR-NKT cells, reflecting their unique roles in the TME.

Similarly, the distribution of cellular sub-clusters across pseudotime demonstrated distinct dynamics between CAR-T and CAR-NKT cells (Fig. 5g). CAR-T cells underwent a pronounced progression, transitioning sharply from proliferating clusters to effector-like clusters, then to memory-like clusters, and predominantly to resting clusters, with small variations across tissues (Fig. 5g). In contrast, CAR-NKT cells displayed a more balanced and stable representation of these clusters across tissues, transitioning gradually from effector-like clusters to memory-like clusters and primarily to resting clusters (Fig. 5g). This steady-state distribution of CAR-NKT cells, characterized by the sustained effector-like and memory-like states, may underpin their ability to maintain antitumor responses over time.

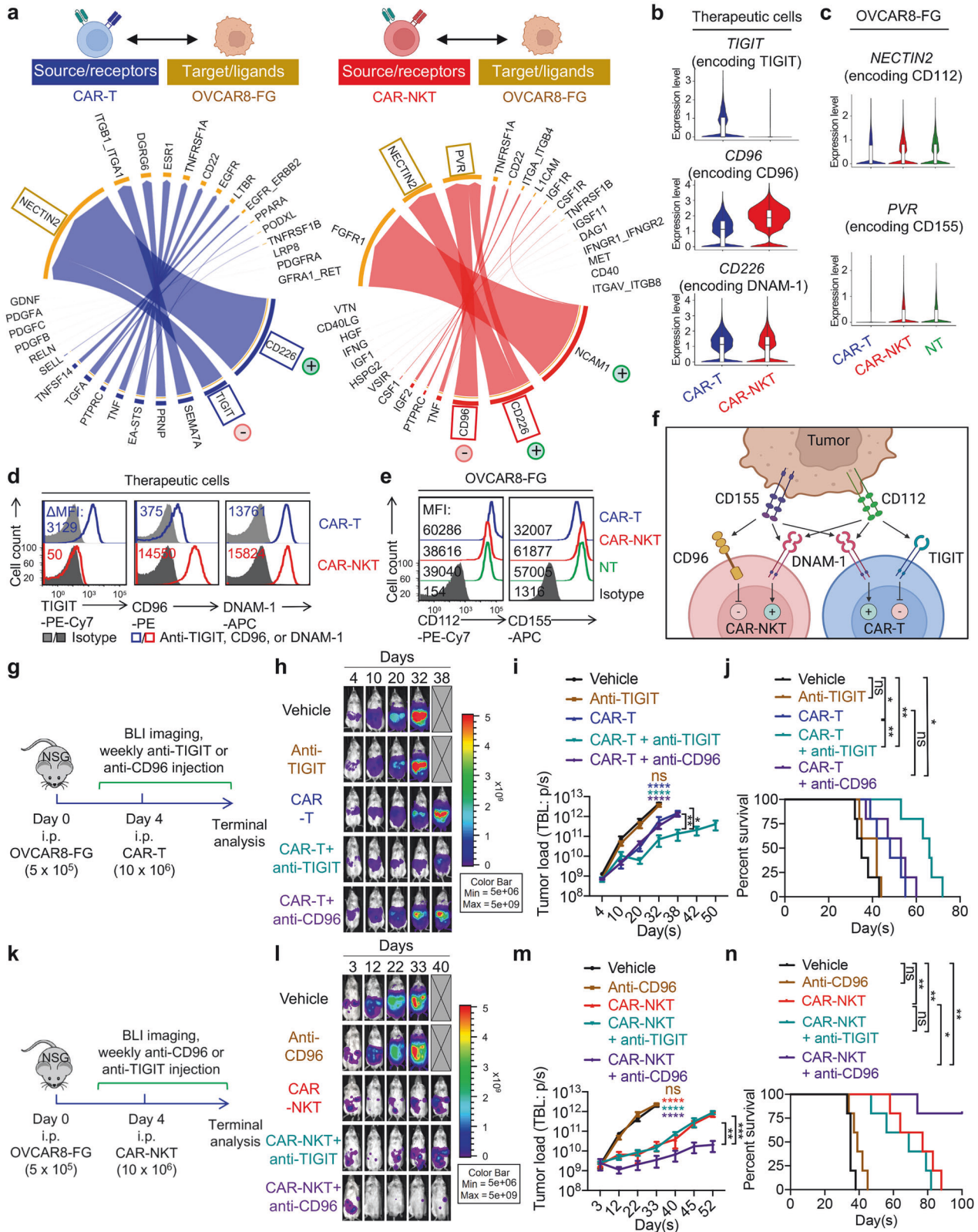
Finally, schematic diagrams summarizing cell state transitions highlighted the divergent progression patterns of CAR-T and CAR-NKT cells (Fig. 5h). While CAR-T cells underwent rapid and distinct transitions to exhaustion, CAR-NKT cells followed a less divergent trajectory, retaining effector and memory phenotypes across

tissues (Fig. 5h). In summary, these results reveal slower cross-tissue equilibrium and less divergent progression of CAR-NKT cells compared to CAR-T cells, underscoring the unique tissue-wide dynamics and differentiation potential of CAR-NKT cells.

Collectively, our comprehensive analyses integrating spatial, temporal, and transcriptional profiling reveal that CAR-T and CAR-NKT cells exhibit markedly distinct behaviors within the solid tumor microenvironment. CAR-T cells demonstrated a rapid proliferation and a pronounced transition toward exhaustion, particularly within the tumor. Their tissue distribution was broad but dynamically unstable, accompanied by reduced differentiation potential and functional decline over time. In contrast, CAR-NKT cells maintained more balanced and sustained metabolic activity, characterized by persistent oxidative phosphorylation and stable amino acid metabolism. They exhibited superior tumor retention, slower pseudotemporal progression, and a sustained presence of effector-like and memory-like states across tissues. Importantly, CAR-NKT cells retained higher differentiation potential and showed limited exhaustion, suggesting enhanced adaptability and long-term persistence in solid tumor settings. These findings underscore fundamental differences in the pharmacodynamic and immunobiological properties of CAR-NKT versus CAR-T cells, and support the strategic development of CAR-NKT cells as a robust platform for next-generation allogeneic immunotherapies against solid tumors.

CAR-NKT cells targeting of solid tumor is regulated by immune checkpoints different from those modulating CAR-T cells. We conducted cell-cell communication analyses covering over 3,200 receptor-ligand pairs on two sets of matched *in vivo* samples: CAR-T cells and their treated OVCAR8-FG tumor cells, as well as CAR-NKT cells and their treated OVCAR8-FG tumor cells (Fig. 6a).³⁷ Significantly different ligand-receptor interactions were discovered among the two sets of samples (Fig. 6a). Between conventional CAR-T cells (source/receptors) and their matched OC tumor cells (target/ligands), the most prominent activating receptor-ligand pair identified was DNAM-1-CD112, whereas the most notable inhibitory pair was TIGIT-CD112 (Fig. 6a–c). In contrast, between CAR-NKT cells (source/receptors) and their matched OC tumor cells (target/ligands), the most significant activating receptor-ligand pairs were DNAM-1-CD112 and DNAM-1-CD155, while CD96-CD155 identified as the prominent inhibitory receptor-ligand pair (Fig. 6a–c).^{38–40} Surface expression of these identified receptor-ligand pairs were further validated on matched therapeutic cells and OC tumor cells using flow cytometry (Fig. 6d–f).

These findings point to the possibility of enhancing the anti-OC efficacy of CAR-T or CAR-NKT cells through blocking their respective critical immune checkpoints. To test this, we utilized the established OVCAR8-FG human OC xenograft mouse model, including the adoptive transfer of two types of therapeutic cells (i.e., CAR-T or CAR-NKT cells) in combination with the administration of two types of immune checkpoint inhibitors (i.e., TIGIT and



CD96 inhibitors) (Fig. 6g–n). A higher dose of OVCAR8-FG tumor cells was injected to prevent complete elimination by CAR-NKT cells, thereby allowing us to distinguish the effects of CAR-NKT cells alone from those of CAR-NKT cells combined with checkpoint blockade (Figs. 1j and 6g, k).

Notably, blockade of TIGIT, but not CD96, resulted in a significant enhancement of the anti-OC efficacy of conventional CAR-T cells, as evidenced by marked tumor suppression and improved animal survival (Fig. 6g–j). TIGIT blockade led to increased CAR-T cell activation at early time points (day 20), as

Fig. 6 CAR-NKT cells targeting of ovarian cancer is regulated by immune checkpoints different from those modulating conventional CAR-T cells. **a–f** Studying the in vivo interplay between CAR-NKT and tumor cells. Peritoneal fluids were collected from the experimental mice at day 28, and the therapeutic cells (identified as human CD45⁺CD3⁺ cells) and OVCAR8-FG tumor cells (identified as GFP⁺ cells) were FACS sorted and subjected to scRNA-seq analyses. The datasets were then combined and analyzed using cell-cell interaction analyses. **a** Chord plots illustrating the top significant ligand-receptor pairs between the indicated therapeutic cell (source) and tumor cell (target) pairs. Violin plots showing the expression of the indicated genes in the therapeutic cells (**b**) or tumor cells (**c**). **d** FACS detection of the indicated immune regulatory receptors on therapeutic cells. **e** FACS detection of the indicated immune regulatory ligands on OVCAR8-FG tumor cells. **f** Schematics showing the interplay between therapeutic cells and tumor cells mediated by the CD96/DNAM-1/TIGIT/CD155/CD112 immune regulatory network. **g–j** Studying the impact of TIGIT or CD96 blockade on anti-tumor efficacy of CAR-T cells in an OVCAR8-FG xenograft mouse model. **g** Experimental design. **h** BLI images. **i** Quantification of (**h**) ($n = 5$). **j** Survival curve ($n = 5$). **k–n** Studying the impact of TIGIT or CD96 blockade on anti-tumor efficacy of CAR-NKT cells in an OVCAR8-FG xenograft mouse model. **k** Experimental design. **l** BLI images. **m** Quantification of (**l**) ($n = 5$). **n** Survival curve ($n = 5$). Representative of 1 (**a–c**) and 3 (**d–n**) experiments. Cells isolated from 5–10 mice of each experimental group were combined for analyses. Data are presented as the mean \pm SEM. ns not significant, * $p < 0.05$, ** $p < 0.01$, *** $p < 0.001$, **** $p < 0.0001$ by one-way ANOVA (**i**, **m**), or by log rank (Mantel-Cox) test adjusted for multiple comparisons (**j**, **n**)

evidenced by upregulation of CD25 and CD69 following anti-TIGIT administration (Supplementary Fig. 10a–d). However, by later time points (day 50), no differences in these activation markers were observed, likely due to extensive CAR-T cell expansion associated with xeno-GvHD (Supplementary Fig. 10a–d). Ultimately, mice succumbed to a combination of tumor relapse and GvHD. In contrast, blockade of CD96, but not TIGIT, significantly augmented the anti-OC efficacy of CAR-NKT cells, associated with suppressed tumor growth and prolonged mouse survival (Fig. 6k–n). Flow cytometric analyses further confirmed that CD96 blockade enhanced CAR-NKT cell persistence, activation, and effector function at both early and late time points, as evidenced by greater numbers of CAR-NKT cells in the peritoneal cavity and elevated expression of CD25 and CD69 (Supplementary Fig. 10e–h). These findings highlight distinct checkpoint dependencies between CAR-T and CAR-NKT cells and provide mechanistic insights into their enhanced antitumor activity under checkpoint blockade.

Given that current checkpoint blockade therapies, particularly those targeting PD-1 and PD-L1, have shown limited clinical benefit in enhancing the efficacy of conventional CAR-T cells for solid tumors, except in cases involving more stem-like CAR-T cell products,¹¹ we assessed the effect of PD-1 blockade on the antitumor efficacy of conventional CAR-T cells using the OVCAR8-FG human OC xenograft mouse model (Supplementary Fig. 11a). Blocking PD-1 did not improve antitumor efficacy of conventional CAR-T cells (Supplementary Fig. 11b–d). The limited effectiveness of PD-1 blockade may be attributed to the low PD-L1 expression on OC tumor cells in the in vivo human OC xenograft mouse models (Supplementary Fig. 11e–k). However, the significantly high expression of other immune checkpoints, such as CD112 and CD155, underscores the necessity of exploring alternative immune checkpoints for CAR cell therapy, including TIGIT and CD96 (Fig. 6 and Supplementary Fig. 11).

Comparison of allogeneic HSPC-derived CAR-NKT cells and clinically used autologous CAR-NKT cells for solid tumor treatment To better understand the biological characteristics of our allogeneic HSPC-derived CAR-NKT cells, we performed a comparative analysis with autologous CAR-NKT cells previously used in a clinical trial for neuroblastoma treatment (Fig. 7a).¹⁸ Although the two CAR-NKT products differ in CAR constructs, disease targets, and experimental models (xenograft model vs. clinical trial), this cross-comparison provides valuable insights that may inform the clinical development of our allogeneic CAR-NKT platform by benchmarking against clinically validated products (Fig. 7a).

Phenotypically, both CAR-NKT cell products exhibited mixed T and NK cell transcriptional features. Notably, our HSPC-derived CAR-NKT cells demonstrated a higher expression of NK-associated gene signatures but lower expression of canonical T cell genes, suggesting a more pronounced NK-like phenotype (Fig. 7b), consistent with prior studies using this manufacturing platform.¹⁶

This enhanced NK-like identity may contribute to their distinct functionality and antitumor capacity.

Despite the differences in origin and culture method, both CAR-NKT cell types exhibited similar in vitro-to-in vivo transcriptional transitions. Upon in vivo exposure, both products upregulated key gene signatures associated with NK-like differentiation (e.g., *KLRB1*, *KLRC1*, and *KLRD1*), cytolytic function (e.g., *GZMH*, *GZMK*, and *NKG7*), and exhaustion (e.g., *BTG1* and *SUB1*), as previously reported in clinical samples (Fig. 7c–e).¹⁶ These findings support the notion that both autologous and HSPC-derived CAR-NKT cells undergo similar differentiation and activation trajectories in vivo, reinforcing their comparable potential for robust antitumor responses.

Further comparative analysis of in vivo cell products revealed that compared to autologous PBMC-derived CAR-NKT cells, HSPC-derived CAR-NKT cells expressed higher levels of effector-related genes (e.g., *CCL5*, *HOPX*, and *PRF1*), memory-associated markers (e.g., *XL1*, *CCR5*, and *CD44*), and cytotoxic mediators (e.g., *GZMH*, *GNLY*, and *NKG7*) (Fig. 7f), highlighting their capacity to execute potent cytolytic and immunomodulatory functions.

Pathway enrichment analysis revealed both shared and distinct regulatory programs. Both in vivo CAR-NKT cell products upregulated pathways related to granzyme-mediated apoptosis, NKT cell differentiation, and NK cell chemotaxis (Fig. 7g). However, the HSPC-derived CAR-NKT cells showed selective enrichment in pathways associated with NK cell degranulation, macrophage homeostasis, and neutrophil activation—functions that may relate to their enhanced innate immune characteristics (Fig. 7g). In contrast, the autologous CAR-NKT cells displayed upregulation of pathways related to T cell tolerance, CD4⁺ T cell proliferation, and lymphocyte homeostasis, indicating more pronounced adaptive immune regulation (Fig. 7g).

In conclusion, this cross-comparison highlights both converging and diverging features between autologous and allogeneic CAR-NKT cell therapies. Our HSPC-derived CAR-NKT cells recapitulate key functional gene programs observed in clinically utilized CAR-NKT cells while exhibiting enhanced NK-like phenotypes and distinct immune regulatory profiles. These findings validate the clinical potential of our allogeneic CAR-NKT platform and support its further development for solid tumor immunotherapy.

Comparison of HSPC-derived and PBMC-derived CAR-NKT cells for solid tumor treatment

We agree that the scRNA-seq analyses revealed similar transcriptional changes between in vitro- and in vivo-expanded CAR-NKT cells; however, there remain significant differences between the two types of CAR-NKT cells (Fig. 7). One key distinction is that HSPC-derived CAR-NKT cells exhibited a stronger NK-related gene signature, together with elevated expression of genes associated with effector, memory, and cytotoxic functions (Fig. 7). To further validate these observations, we generated healthy donor PBMC-derived CAR-NKT cells engineered with the same CAR construct

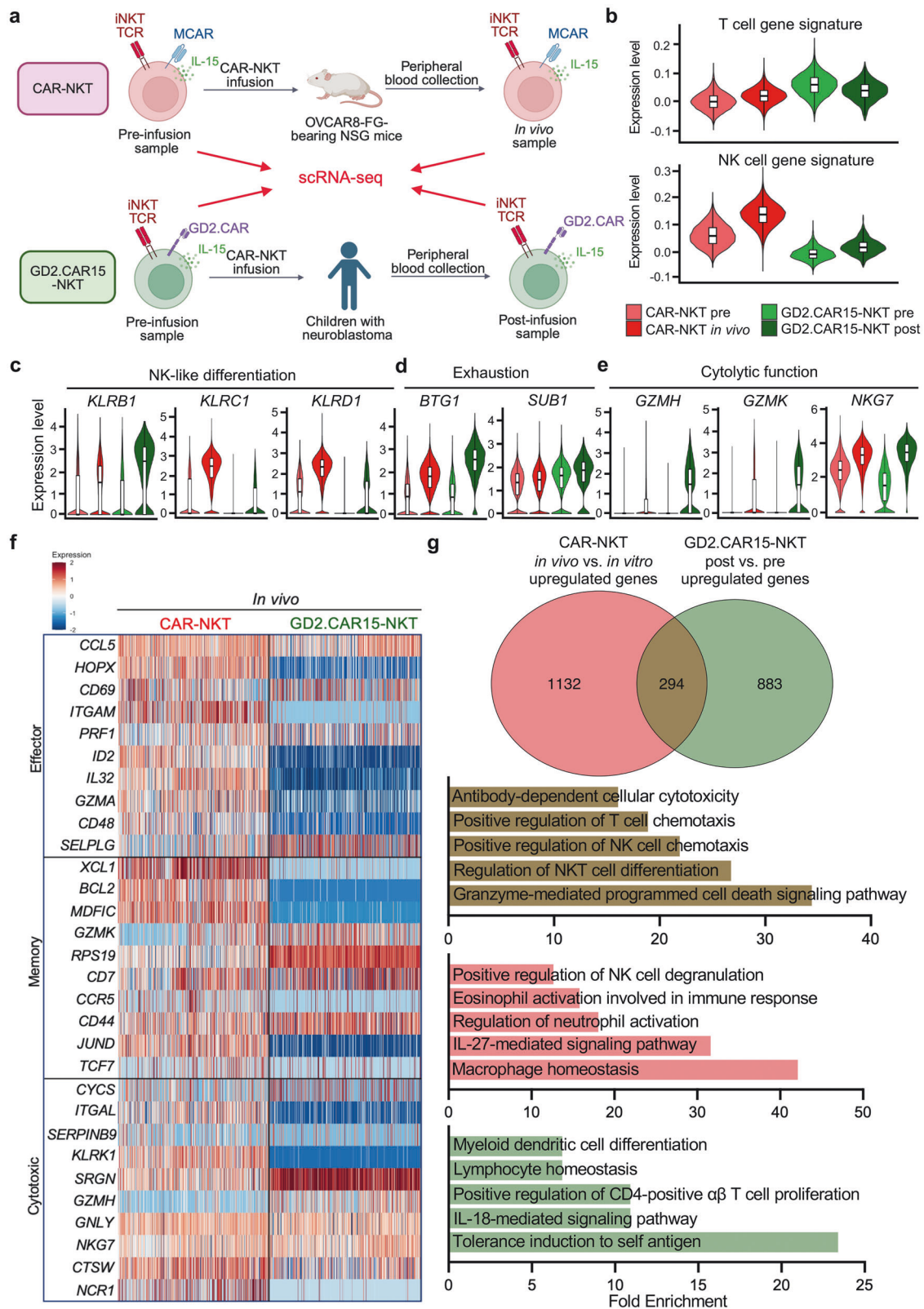


Fig. 7 Comparison of allogeneic HSPC-derived CAR-NKT cells and clinically used autologous CAR-NKT cells for solid tumor treatment. **a** scRNA comparison between HSPC-derived CAR-NKT cells and PBMC-derived IL-15-enhanced GD2CAR-engineered NKT (GD2-CAR15 NKT) cells. GD2-CAR15 NKT cell data are obtained from GSE223071. **b** Violin plots showing the expression distribution of T and NK cell gene signatures in the indicated CAR-NKT cells. Violin plots showing the expression distribution of genes involved in NK-like differentiation (**c**), exhaustion (**d**) and cytolytic function (**e**), in the indicated CAR-NKT cells. **f** Heatmap showing the expression of representative signature genes. Each column indicates an individual cell. Each row indicates an individual gene. **g** Venn diagram showing the numbers of shared and unique pathways of HSPC-derived and PBMC-derived CAR-NKT cell samples. The Pathway analyses were conducted by comparing differentially expressed genes between post-tumor cell challenge samples and pre-infusion samples. The indicated pathway in each category are shown in the bar plots

and soluble IL-15 (hereafter referred to as ^{PBMC}CAR-NKT cells), and performed side-by-side comparisons between HSPC-derived and PBMC-derived CAR-NKT cells, including assessments of their phenotype, functionality, and in vitro and in vivo antitumor activity.

^{PBMC}CAR-NKT cells were generated using a well-established protocol.^{16,41} NKT cells were isolated from PBMCs, activated using irradiated α GC-loaded PBMCs to provide TCR stimulation, and transduced with Lenti/MCAR-IL15 lentiviruses (Supplementary Fig. 12a). After 2-3 weeks of culture, we obtained ^{PBMC}CAR-NKT cells with high purity (>96%), robust expansion (>700-fold), and substantial CAR expression (~60%). These CAR⁺ cells were further purified by flow sorting and used for subsequent experiments (Supplementary Fig. 12b–d).

Phenotypic comparison revealed that HSPC-derived CAR-NKT cells were dominated by CD8 single-positive (SP) and double-negative (DN) subsets, with a near absence of CD4 SP cells, which is consistent with patterns observed in other stem cell-derived allogeneic T cell products (Supplementary Fig. 12e).^{42–44} In contrast, ^{PBMC}CAR-NKT cells contained all three subpopulations (CD4 SP, CD8 SP, and DN), representing a more balanced composition that includes CD4⁺ helper and regulatory subsets (Supplementary Fig. 12e).

When assessing proliferation, HSPC-derived CAR-NKT cells exhibited significantly higher Ki-67 expression compared to ^{PBMC}CAR-NKT cells, indicating greater proliferative activity and self-renewal potential, which may contribute to their enhanced persistence in vivo (Supplementary Fig. 12f, g).

Intracellular cytokine staining further revealed distinct functional polarization between the two CAR-NKT cell types. HSPC-derived CAR-NKT cells displayed a Th1-biased cytokine profile, characterized by high levels of IFN- γ , TNF- α , and IL-2, but minimal production of Th2- or Th17-associated cytokines (Supplementary Fig. 12h). In contrast, ^{PBMC}CAR-NKT cells produced a broader cytokine spectrum, including lower Th1 cytokines and significantly higher levels of IL-4 and IL-17, reflecting a mixed Th1/Th2/Th17 phenotype (Supplementary Fig. 12h). These results suggest that HSPC-derived CAR-NKT cells favor a proinflammatory and cytotoxic functional state, while PBMC-derived cells maintain a more heterogeneous immune profile that may include immunoregulatory functions.^{35,45–47}

Given that scRNA-seq analyses indicated enhanced NK-like features in HSPC-derived CAR-NKT cells, we next examined the expression of NKR and NK-associated markers, and assessed their contribution to tumor cell killing. HSPC-derived CAR-NKT cells expressed markedly higher levels of NKG2D, DNAM-1, NKp44, NKp30, and CD56 compared to ^{PBMC}CAR-NKT cells (Supplementary Fig. 12i). In 24-hour in vitro tumor cell killing assays, both cell types effectively lysed MSLN⁺ tumor cells (OVCAR8-FG and OVCAR3-FG), but HSPC-derived CAR-NKT cells demonstrated superior cytotoxic capacity (Supplementary Fig. 12j, k). Notably, against MSLN⁻ tumor cells (SKOV3-FG and OVCAR3-FG^{MSLN^{-/-}}), only HSPC-derived CAR-NKT cells achieved robust killing, indicating their ability to mediate NKR-dependent, antigen-independent cytotoxicity, which PBMC-derived CAR-NKT cells lacked (Supplementary Fig. 12j, k). Therefore, HSPC-derived CAR-NKT cells possess a dual tumor recognition capacity, through both CAR- and NKR-mediated mechanisms, allowing them to target antigen-low or antigen-loss tumor variants.

We further compared the two CAR-NKT cell types using a long-term tumor killing assay. Both HSPC-derived and ^{PBMC}CAR-NKT cells maintained sustained tumor control for up to 20 days, likely supported by autocrine IL-15 expression, which promotes long-term persistence and functionality (Supplementary Fig. 12l, m). However, HSPC-derived CAR-NKT cells exhibited superior tumor control at later stages, coinciding with lower expression of exhaustion markers, including PD-1, CTLA-4, TIM-3, LAG-3, and TIGIT (Supplementary Fig. 12m, n). These findings indicate that

HSPC-derived CAR-NKT cells maintain a less exhausted, more functionally durable phenotype, enabling prolonged antitumor activity.

In vivo, we evaluated their therapeutic efficacy using a SKOV3-FG human ovarian cancer xenograft model, which expresses low levels of MSLN, thereby mimicking antigen-escape or low-antigen-density tumor settings (Supplementary Fig. 12o). ^{PBMC}CAR-NKT cells achieved moderate tumor growth suppression and modestly extended mouse survival (Supplementary Fig. 12p–r). In contrast, HSPC-derived CAR-NKT cells exhibited potent antitumor activity, resulting in significantly improved tumor regression and prolonged survival (Supplementary Fig. 12p–r). These results demonstrate that HSPC-derived CAR-NKT cells are highly effective against solid tumors with heterogeneous or low antigen expression, owing to their enhanced NK-like and cytotoxic properties.

Overall, HSPC-derived CAR-NKT cells combine the advantages of robust proliferation, potent cytotoxicity, NKR-mediated antigen-independent tumor killing, and resistance to exhaustion, leading to durable in vivo antitumor efficacy. These findings highlight the therapeutic potential of HSPC-engineered CAR-NKT cells as a powerful and versatile allogeneic cell therapy platform capable of overcoming the challenges of antigen heterogeneity and immune escape in solid tumors.

DISCUSSION

Here, we represent a comprehensive, high-resolution analysis of human CAR-T and CAR-NKT cell therapies against solid tumors, delivering novel insights into their divergent in vivo dynamics and regulatory mechanisms. By integrating scRNA-seq with in vivo functional validation, we constructed a unique spatiotemporal map of engineered immune cells as they engage with solid tumor microenvironments and disseminate across host tissues. This approach allowed us to simultaneously assess gene expression, tissue distribution, and checkpoint regulation at single-cell resolution and at multiple time points during therapy. Specifically, we analyzed more than 80 tumor-bearing mice, sampled from 4 tissue compartments over 5 time points, and profiled a total of 274,878 individual cells (Fig. 3a). The breadth and depth provided a comprehensive landscape of the cellular states, inter-compartmental kinetics, and molecular signatures associated with CAR-T and CAR-NKT therapy, revealing how these therapeutic modalities behave and adapt within the complex in vivo context of solid tumors (Fig. 3b–f). Our work, therefore, not only addresses a major gap in knowledge but also provides a rich resource for informing rational design and clinical translation of CAR engineered immune cells.

One of the key contributions of this study lies in elucidating the in vivo PK/PD profiles of human CAR-T versus CAR-NKT cells, highlighting distinct patterns of tissue localization, persistence, and safety (Fig. 2a). We found that CAR-NKT cells demonstrated highly localized infiltration into tumor tissues, with negligible presence in healthy organs even at late time points (Fig. 2b–d). This constrained distribution pattern is a desirable feature for cancer immunotherapy, as it minimizes on-target, off-tumor damage to normal tissues while concentrating cytotoxic effects at the tumor site (Fig. 2e–g).²⁷ In contrast, CAR-T cells displayed more diffuse infiltration across multiple organs, consistent with their broader tissue-homing potential but also indicative of a higher risk of systemic toxicity (Fig. 2b–g). This distinction was further underscored by our transcriptomic analyses, which revealed that CAR-NKT cells maintained a more stable and balanced gene expression program across both tumor and non-tumor compartments (Fig. 5a, b). CAR-NKT cells preserved effector-like and memory-like phenotypes with relatively uniform functional states across tissues over time (Fig. 5c–h). In contrast, CAR-T cells exhibited marked inter-tissue divergence and dynamic instability, characterized by abrupt shifts toward effector and

exhaustion-like states within the tumor and spleen (Fig. 5a, b), as well as increased activation signatures and loss of differentiation potential over pseudotime (Fig. 5c–h). These preclinical findings mirror clinical reports in which mesothelin-targeted CAR-T therapies in cancer patients have resulted in severe, sometimes fatal pulmonary toxicities due to off-tumor targeting of mesothelin-expressing normal tissues.²⁷ Building on these preclinical observations, it will be essential for future studies to comprehensively evaluate the safety profile of CAR-NKT cells in clinical settings, including their tissue-specific localization, persistence, and potential off-tumor effects, to ensure both efficacy and tolerability in patients.

Importantly, we also demonstrated that CAR-NKT cells can be efficiently derived from allogeneic cord blood-derived HSPC source (Fig. 1a–c), enabling the generation of standardized, “off-the-shelf” therapeutic products that not only retain but enhance safety and efficacy compared to traditional approaches (Fig. 1d–i). Notably, in our head-to-head *in vivo* comparisons, CAR-NKT cells exhibited superior cytotoxic antitumor activity relative to CAR-T cells, achieving more robust tumor control (Fig. 1j–m). Furthermore, metabolic profiling revealed that CAR-NKT cells maintained stable oxidative phosphorylation, electron transport, and amino acid metabolism, reflecting their superior metabolic fitness and adaptability within the TME (Fig. 4a–f). By contrast, CAR-T cells showed progressive metabolic decline, particularly in amino acid metabolism, consistent with functional exhaustion and diminished effector capacity (Fig. 4a–f).

Blocking immune checkpoints is an attractive avenue to improve CAR-T cell therapy for solid tumors. However initial clinical trials evaluating PD-1/PD-L1 and CTLA-4 blockade in combination with conventional CAR-T cells have not demonstrated therapeutic benefit in solid tumors. Our study profiled the “*in vivo*, *in action*” ligand-receptor pairs between solid tumor cells and therapeutic cells and found that the PD-1/PD-L1 pair was not a significant player in the solid tumor microenvironment, potentially explaining the limited efficacy of PD-1/PD-L1 blockade in this context (Fig. 6a–f). Subsequently, our study identified TIGIT as the key immune checkpoint regulating CAR-T cells, while CD96 as the key immune checkpoint regulating allogeneic CAR-NKT cells, validated by both *in vivo* human xenograft mouse models and primary patient sample analyses (Fig. 6g–n and Supplementary Figs. 10 and 11). These findings highlight the importance of tailoring immune checkpoint blockade strategies to specific therapeutic cell types and suggest the promise of harnessing TIGIT and CD96 blockades to enhance cell therapy for solid tumors.

Despite the strengths of our study, we acknowledge several limitations that warrant consideration. One limitation relates to the use of allogeneic HSPC-derived CAR-NKT cells in our experiments, which may exhibit differences from CAR-T or CAR-NKT cells derived from PBMCs in terms of developmental cues, functional properties, and *in vivo* persistence.¹⁶ Indeed, our comparative analyses revealed notable differences between the allogeneic HSPC-derived CAR-NKT cells developed in this study and previously reported autologous PBMC-derived CAR-NKT cells,¹⁸ particularly in functional gene expression profiles (Fig. 7a–g). These differences likely arise from a combination of intrinsic biological distinctions between stem cell-derived and PBMC-derived NKT cells, as well as extrinsic factors related to manufacturing processes, including differences in CAR constructs, culture conditions, and differentiation trajectories.^{16,18,48} Nevertheless, it is important to emphasize that our primary focus was not to exhaustively characterize CAR-T cell biology, but rather to provide a mechanistic and translational understanding of CAR-NKT cell biology and its unique *in vivo* behavior as a therapeutic platform. We recognize that future studies will be needed to dissect the contributions of donor source, cell differentiation state, and manufacturing conditions to therapeutic outcomes. However,

the central message of our work remains: CAR-NKT cells exhibit a distinct *in vivo* profile that is favorable for solid tumor therapy and warrants further clinical development as a next-generation cell-based therapeutic strategy.

In addition, in the current study, all scRNA-seq analyses were conducted in an ovarian cancer xenograft model, in which both tumor cells and the TME are localized in the peritoneal cavity, thereby representing peritoneal disease. Therefore, in other solid tumors with similar physiological features, such as gastric cancer and peritoneal mesothelioma, the phenotype and functionality of allogeneic CAR-NKT cells are expected to be comparable. In contrast, in solid tumors with distinct TME characteristics, the behavior of therapeutic cells may differ. For example, it has been observed that CAR-T cells exhibit increased exhaustion and reduced effector function in immunologically ‘cold’ TMEs, such as those found in breast cancer, prostate cancer, and glioblastoma. Further investigation of CAR-NKT cell activity across different solid tumor contexts is therefore warranted. Of note, since MSLN is also expressed in other malignancies, including pancreatic cancer, breast cancer, lung cancer, and others, the same MSLN-targeting CAR-NKT cell product could potentially be applied to these indications. However, their *in vivo* phenotype and functionality, particularly at the transcriptomic level, may vary across tumor types and require further exploration.

When evaluating xeno-GvHD, which refers to GvHD-like symptoms induced by human CAR-T cells in xenograft mouse models, we recognize that this phenomenon does not fully recapitulate the clinical context of allogeneic GvHD in patients. A more physiologically relevant approach would involve the use of humanized NSG mice reconstituted with human CD34⁺ hematopoietic stem cells, which better mimic human immune system interactions and the clinical manifestations of GvHD.^{49,50} Although xeno-GvHD is less clinically meaningful, it remains a valuable preclinical model to assess immune cell-mediated toxicity and to compare the alloreactive potential between different engineered cell types. In this context, our findings highlight a clear distinction between CAR-T and CAR-NKT cells: whereas CAR-T cells induced pronounced xeno-GvHD symptoms, CAR-NKT cells did not, underscoring their favorable safety profile and reduced alloreactivity (Fig. 2). Future studies employing humanized NSG models will be instrumental in further validating these observations and elucidating the mechanisms underlying the immune tolerance and persistence of CAR-NKT cells in a more clinically relevant setting.

Lastly, the checkpoint pathways identified in our study have significant implications for the future of CAR-NKT-based cancer immunotherapy, aligning with the broader, emerging trend of using genetic engineering to enhance the efficacy and durability of adoptive cell therapies. Recent advances in genome editing have already demonstrated success in improving cell products by disrupting inhibitory pathways in other platforms, such as iPSC-derived NK cells and conventional PBMC-derived CAR-T cells, where targeted CRISPR/Cas9-mediated knockouts of inhibitory receptors have been employed to overcome tumor-induced suppression and boost antitumor activity. In this context, our identification of distinct checkpoint regulators specific to CAR-NKT cells, such as CD96, provides a compelling rationale to extend these engineering strategies to the CAR-NKT platform. Targeted knockout of these inhibitory pathways could further enhance the persistence, cytotoxicity, and overall therapeutic potency of CAR-NKT cells while preserving their favorable safety profile. Moreover, our spatiotemporal profiling framework offers a versatile platform to discover additional actionable pathways and to rationally design combinatorial engineering and checkpoint blockade strategies tailored to CAR-NKT cell biology. In sum, our findings not only highlight the unique regulatory circuitry of CAR-NKT cells but also position them squarely within the next wave of engineered immunotherapies, offering a roadmap for iterative

improvement through rational design, precise gene editing, and integration with checkpoint-targeted approaches.

MATERIALS AND METHODS

Detailed descriptions of cell lines, human cord blood CD34⁺ hematopoietic stem and progenitor cells (HSPCs) and periphery blood mononuclear cells (PBMCs), media and reagents, lentiviral vectors, generation of allogeneic mesothelin-targeting CAR-engineered NKT (CAR-NKT) cells, generation of MSLN-targeting CAR-engineered conventional $\alpha\beta$ T (CAR-T) cells, generation of PBMC-derived MSLN-targeting CAR-engineered NKT (P^{BMC}CAR-NKT) cells, and in vitro scanning electron microscope (SEM), are provided in the Supplementary Materials file.

Mice

NOD.Cg-Prkdc^{SCID}Il2rg^{tm1Wjl}/SzJ (NOD/SCID/IL-2R γ ^{-/-}, NSG) mice purchased from The Jackson Laboratory (Strain #005557, RRID: IMSR_JAX:005557) and maintained in the University of California, Los Angeles (UCLA) animal facilities were used at 6-10 weeks of age unless noted otherwise. Both male and female mice were included in this study, and no significant sex-based differences were observed in the preclinical human tumor xenograft models. All mice were housed under specific pathogen-free conditions. All procedures were approved by the UCLA Institutional Animal Care and Use Committee (IACUC) and conducted in accordance with guidelines from the UCLA Division of Laboratory Animal Medicine (DLAM).

Antibodies and flow cytometry

Fluorochrome-conjugated antibodies specific for human CD45 (Clone HI30, PerCP, FITC or Pacific Blue-conjugated, 1:500, cat. no. 304025, 304005, or 304021, RRID: AB_893341, AB_314393, or AB_493654), TCR $\alpha\beta$ (Clone IP26, Pacific Blue or PE-Cy7-conjugated, 1:25, cat. no. 306715 or 306719, RRID: AB_1953256 or AB_10640829), CD3 (Clone HIT3a, Pacific Blue, PE, or PE-Cy7-conjugated, 1:500, cat. no. 300330, 300308, or 300316, RRID: AB_10551436, AB_314044, or AB_314052), CD4 (Clone OKT4, PE-Cy7, PerCP, or FITC-conjugated, 1:500, cat. no. 317414, 317432, or 317408, RRID: AB_571959, AB_2028494, or AB_571951), CD8 (Clone SK1, PE, APC-Cy7, or APC-conjugated, 1:300, cat. no. 980902, 344713, or 344721, RRID: AB_2616623, AB_2044005, or AB_2075390), CD45RO (Clone UCHL1, PE, APC-Cy7, or APC-conjugated, 1:100, cat. no. 304206, 304228, or 304210, RRID: AB_314422, AB_10895897, or AB_314426), CD161 (Clone HP-3G10, FITC, PE, or APC-conjugated, 1:50, cat. no. 339906, 339904, or 339912, RRID: AB_2234362, AB_1501083, or AB_10900826), CD56 (clone QA18A21, APC-Cy7, APC, or PE-conjugated, 1:20, cat. no. 398813, 398805, or 398803, RRID: AB_3097438, AB_2894509, or AB_2820070), CD14 (Clone HCD14, PE, PerCP, or FITC-conjugated, 1:100, cat. no. 325606, 325632, or 325604, RRID: AB_830679, AB_2563328, or AB_830677), CD69 (Clone FN50, PE-Cy7 or PerCP-conjugated, 1:50, cat. no. 310911 or 310927, RRID: AB_314846 or AB_10696423), CD62L (Clone DREG-56, PE, APC, or FITC-conjugated, 1:50, cat. no. 304806, 304810, or 304804, RRID: AB_314466, AB_314470, or AB_314464), CD107a (Clone H4A3, FITC or PE-conjugated, 1:100, cat. no. 328606 or 328608, RRID: AB_1186036 or AB_1186040), CD1d (clone 51.1, PE-Cy7 or APC-conjugated, 1:50, cat. no. 25-0016-42 or 17-0016042, RRID: AB_2815094 or AB_11219079), CD11b (Clone ICRF44, APC or PE-conjugated, 1:500, cat. no. 301310 or 301306, RRID: AB_314162 or AB_314158), CD11c (Clone Bu15, PE or FITC-conjugated, 1:200, cat. no. 337206 or 337214, RRID: AB_1236405 or AB_2129792), CD206 (Clone 15-2, PE or FITC-conjugated, 1:500, cat. no. 321106 or 321104, RRID: AB_571911 or AB_571905), CD163 (Clone GHI/61, PerCP or PE-conjugated, 1:500, cat. no. 333626 or 333606, RRID: AB_2650630 or AB_1134002), NKG2D (Clone 1D11, PE-Cy7-conjugated, 1:50, cat. no. 320811, RRID: AB_2133275), DNAM-1

(Clone 11A8, APC-conjugated, 1:50, cat. no. 338311, RRID: AB_2561951), β 2-microglobulin (B2M) (Clone 2M2, PE or FITC-conjugated, 1:5000, cat. no. 316306 or 316304, RRID: AB_492839 or AB_492837), HLA-DR, DP, DQ (Clone T α 39, APC or PE-conjugated, 1:250, cat. no. 361714 or 361716, RRID: AB_2750316 or AB_2750318), HLA-A,B,C (Clone W6/32, APC or FITC-conjugated, 1:1000, cat. no. 311410 or 311404, RRID: AB_314879 or AB_314873), MICA/B (Clone 6D4, APC-conjugated, 1:25, cat. no. 320907, RRID: AB_493196), IFN- γ (Clone B27, PE-Cy7-conjugated, 1:50, cat. no. 506517, RRID: AB_2123322), TNF- α (Clone MAb11, FITC or APC-conjugated, 1:1000, cat. no. 502906 or 502912, RRID: AB_315258 or AB_315264), IL-2 (Clone MQ1-17H12, APC-Cy7-conjugated, 1:50, cat. no. 500341, RRID: AB_2562854), Granzyme B (Clone QA16A02, APC or FITC-conjugated, 1:5000, cat. no. 372204 or 372206, RRID: AB_2687028 or AB_2687030), Perforin (Clone dG9, PE-Cy7-conjugated, 1:50 or 1:100, cat. no. 308125, RRID: AB_2572048), Streptavidin (Clone 3A20.2, PE-conjugated, 1:1000, cat. no. 410504, RRID: AB_2571915), PD-1 (Clone A17188A, FITC, APC, or PE-conjugated, 1:50, cat. no. 379205, 379207, or 379209, RRID: AB_2922605, AB_2922606, or AB_2922607), LAG-3 (Clone 11C3C65, FITC, APC-Cy7, or PE-conjugated, 1:50, cat. no. 369307, 369347, or 369305, RRID: AB_2629750, AB_2922585, or AB_2629591), TIM-3 (Clone A18087E, PE or APC-conjugated, 1:50, cat. no. 364805 or 364803, RRID: AB_2922577 or AB_2910409), TIGIT (Clone A15153G, PE, APC, or APC-Cy7-conjugated, 1:50, cat. no. 372703, 372705, or 372733, RRID: AB_2632729, AB_2632731, or AB_2876700), CTLA-4 (Clone BNI3, PE-Cy7 or APC-Cy7-conjugated, 1:50, cat. no. 369613 or 369633, RRID: AB_2632875 or AB_2892451), Ki-67 (Clone Ki-67, APC-conjugated, 1:200, cat. no. 350514, RRID: AB_10959327), CCR1 (Clone 5F10B29, PE-conjugated, 1:50, cat. no. 362904, RRID: AB_2563898), CCR5 (Clone J418F1, FITC-conjugated, 1:50, cat. no. 359120, RRID: AB_2564071), CXCR3 (Clone G025H7, APC-conjugated, 1:200, cat. no. 353708, RRID: AB_10983064), CXCR6 (Clone K041E5, PE-Cy7-conjugated, 1:50, cat. no. 356012, RRID: AB_2562315), CCR7 (Clone G043H7, APC-conjugated, 1:100, cat. no. 353214, RRID: AB_10917387) were purchased from BioLegend. Fluorochrome-conjugated antibodies specific for human mesothelin (Clone 420411, PE-conjugated, 1:10, cat. no. FAB32652P, RRID: AB_1151946), fibroblast activation protein alpha (FAP; Clone 427819, PE-conjugated, 1:100, cat. no. FAB3715P-100, RRID: AB_3086725), ULBP-1 (Clone 170818, PE-conjugated, 1:25, cat. no. FAB1380P, RRID: AB_2687471), and ULBP-2,5,6 (Clone 165903, APC-conjugated, 1:25, cat. no. FAB1298A, RRID: AB_2257142) were purchased from R&D Systems. Fluorochrome-conjugated antibodies specific for mouse CD45 (Clone QA17A26, PE or APC-conjugated, 1:200, cat. no. 157604 or 157606, RRID: AB_2876536 or AB_2876537), F4/80 (Clone BM8, PE or FITC-conjugated, 1:100, cat. no. 123110 or 123108, RRID: AB_893486 or AB_893502), CD11b (Clone M1/70, APC or FITC-conjugated, 1:200, cat. no. 101212 or 101206, RRID: AB_312795 or AB_312789), Gr-1 (Clone RB6-8C5, PE or APC-conjugated, 1:200, cat. no. 108408 or 108412, RRID: AB_313373 or AB_313377), IgG2b, κ Isotype control (Clone MG2b-57, FITC or PE-conjugated, 1:50, cat. no. 401206 or 401208, RRID: AB_2783641 or AB_326637) were purchased from BioLegend. Fluorochrome-conjugated antibodies specific for human TCR Va24-J β 18 (Clone 6B11, PE-conjugated, 1:25, cat. no. 748828, RRID: AB_2873231) were purchased from BD Biosciences. Fixable Viability Dye eFluor506 (e506; 1:500, cat. no. 65-0866-18) was purchased from Affymetrix eBioscience. Human Fc Receptor Blocking Solution (TruStain FcX, 1:100, cat. no. 422302, RRID: AB_2818986) was purchased from BioLegend, and Mouse Fc Block (anti-mouse CD16/32, Clone 2.4G2, 1:50, cat. no. 553141, RRID: AB_394656) was purchased from BD Biosciences. The DAPI Solution and the goat anti-mouse IgG F(ab')₂ secondary antibody (HRP-conjugated, 1:50, cat. no. 31436, RRID: AB_228313) were purchased from Invitrogen. A fluorochrome-conjugated antibody specific for human V β 11 (clone C21, APC-conjugated, 1:50, cat. no. A66905, RRID: AB_3683578) was purchased from Beckman-

Coulter. In our study, note the use of antibodies with identical clones but differing conjugated fluorochromes, with one typical antibody listed herein.

Most flow cytometry stains were performed in PBS for 15 min at 4 °C. The samples were stained with e506 mixed with Mouse Fc Block (anti-mouse CD16/32) or Human Fc Receptor Blocking Solution (TrueStain FcX) prior to antibody staining. Antibody staining was performed at a dilution according to the manufacturer's instructions. For intracellular cytokine staining, cells were stimulated with Phorbol-12-myristate-13-acetate (PMA) and Ionomycin for 2 hours, followed by the addition of GolgiStop Protein Transport Inhibitor, and further incubated for 4 hours. The cells were then stained using a Cell Fixation/Permeabilization Kit (BD Biosciences, cat. no. 554714, RRID: AB_2869008). For the degranulation marker CD107a staining, cells were initially treated with an anti-human CD107a antibody, followed by a 2-hour incubation, and subsequent collection and staining with other antibodies. Stained cells were analyzed using a MACSQuant Analyzer 10 flow cytometer (Miltenyi Biotech), following the manufacturer's guidelines. FlowJo software version 9 (BD Biosciences) was used for data analysis.

In vitro tumor cell killing assay

Tumor cells were plated at 1×10^4 cells per well and incubated with the indicated therapeutic effector cells (CAR-NKT or CAR-T) in Corning 96-well black plates with clear bottoms in C10 medium. Co-cultures were maintained for 24 hours, using effector-to-target (E:T) ratios specified in the corresponding figures or figure legends. Following incubation, tumor cell viability was assessed by the addition of D-luciferin (150 $\mu\text{g}/\text{mL}$; Caliper Life Sciences), and luminescence was measured using an Infinite M1000 microplate reader (Tecan) to quantify luciferase activity from viable tumor cells.

To study the NKR-mediated tumor cell killing in vitro, 10 $\mu\text{g}/\text{mL}$ Ultra-LEAFTM purified anti-human NKG2D (Clone 1D11, cat. no. 320814, RRID: AB_2561488, BioLegend), anti-human DNAM-1 antibody (Clone 11A8, cat. no. 338302, RRID: AB_1279155, BioLegend), or Ultra-LEAFTM purified mouse IgG2bk isotype control antibody (Clone MG2B-57, cat. no. 401217, RRID: AB_3097073, BioLegend) was added to co-cultures one hour prior to adding CAR-NKT cells.

In vitro long-term tumor cell killing assay

A total of 1×10^4 non FG-engineered tumor cells (e.g., OVCAR3 cells; referred to as stimulator cells) was cocultured with 2×10^5 therapeutic cells (e.g., CAR-NKT cells) in a Corning 96-well clear bottom black plate in C10 medium. Cultures were supplemented with a dose of 1×10^4 stimulator cells every 2 days. 24 h prior to luminescent tumor killing readout, stimulator cells were substituted with 1×10^4 of FG-engineered tumor cells (e.g., OVCAR3-FG cells; referred to as indicator cells). To quantify the remaining live indicator cells, 100 μL of D-luciferin (150 $\mu\text{g}/\text{mL}$) was added to cell cultures on the day of imaging and the luciferase activities were measured through readout with an Infinite M1000 microplate reader (Tecan).

Metabolites extraction

Metabolite extraction was performed on 5×10^5 CAR-T and CAR-NKT cells. First, the media was completely aspirated from each sample, followed by a gentle wash with 2 mL of ice-cold ammonium acetate. After aspirating as much ammonium acetate as possible, 500 μL of 80% methanol solution was added to each sample. The cells were then placed on dry ice for 15 minutes, after which all tubes were vortexed vigorously for 20 seconds. The samples were centrifuged at $17,000 \times g$ for 10 minutes at 4 °C, and 250 μL of the supernatant was carefully transferred to new 2 mL tubes for evaporation. The tubes were then placed in a nitrogen

evaporator (Organomation) until all liquid was removed. Finally, the dried samples were stored at -80 °C until further analysis.

Metabolite measurement by liquid chromatography-mass spectrometry (LC-MS)

Dried metabolites were reconstituted in 100 μL of 50% acetonitrile. Following resuspension, the samples were vortexed briefly and centrifuged at $17,000 \times g$ for 10 minutes. A total of 75 μL of the resulting supernatant was transferred into HPLC glass vials for analysis. Metabolite separation was performed using a Vanquish UHPLC system (Thermo Scientific) equipped with a SeQuant ZIC-pHILIC Polymeric column (2.1 \times 150 mm, 5 μm ; EMD Millipore) maintained at 35 °C. The mobile phases consisted of 20 mM ammonium carbonate (pH 9.7) as solvent A and 100% acetonitrile as solvent B, with a flow rate of 150 $\mu\text{L}/\text{min}$ and an injection volume of 10 μL . Chromatographic separation was achieved using a linear gradient from 20% to 80% solvent A over 20 minutes, followed by a rapid return to 20% solvent A between 20 and 20.5 minutes, and a hold at 20% solvent A until 28 minutes. The UHPLC system was coupled to a Q Exactive mass spectrometer (Thermo Scientific) operating in polarity-switching mode. Instrument parameters were set as follows: spray voltage 3.2 kV; sheath gas 40; auxiliary gas 15; sweep gas 1; auxiliary gas temperature 350 °C; and capillary temperature 275 °C. Full-scan MS data were acquired for both positive and negative ion modes over an m/z range of 70–1000, with a resolution of 70,000, a maximum injection time of 250 ms, and an AGC target of 1×10^6 . Data-dependent MS/MS spectra were collected for the three most abundant singly charged ions per scan using a normalized collision energy of 35.

Metabolomic data analysis

The resulting raw files were centroided and converted into mzXML format (separate files for positive and negative modes) using the msconvert tool from ProteoWizard. Ion chromatograms were generated from MS1 spectra using MZmine 2 through the integrated Automated Data Analysis Pipeline (ADAP) chromatogram module. Peak detection was conducted using the ADAP wavelets algorithm, and the resulting features were aligned across all samples employing the Random Sample Consensus (RANSAC) aligner. Following alignment, peaks were gap-filled and annotated based on exact mass (± 15 ppm) and retention time (± 0.5 min) matching against an in-house MS1–RT database comprising 178 authenticated metabolite standards. Peak boundaries and metabolite annotations were subsequently refined through manual curation. Quantification was performed by integrating the area under the chromatographic peak. Metabolite ratios were determined using corresponding peak area values.

In vivo bioluminescence live animal imaging (BLI)

In vivo BLI was conducted using a Spectral Advanced Molecular Imaging (AMI) HTX system (Spectral Instruments Imaging). Mice were anesthetized and imaged 5 minutes after intraperitoneal administration of D-luciferin. For detection of tumor-associated signals (e.g., OVCAR8-FG cells), D-luciferin was administered at a dose of 1 mg per mouse, whereas a higher dose of 3 mg per mouse was used to visualize therapeutic cell populations (e.g., CAR-NKT/FG cells). Acquired images were processed and quantified using AURA imaging software (Spectral Instruments Imaging, version 3.2.0). When quantifying BLI signals in mice, particularly to distinguish therapeutic cells localized in the peritoneal cavity (PC) from those in other tissues, we first defined a region of interest (ROI) encompassing the peritoneal cavity and recorded the corresponding BLI signal. To calculate the signal from other tissues (denoted as "Other"), we quantified the total whole-body BLI signal and subtracted the peritoneal cavity value. It is important to note that the peritoneal cavity ROI includes the

gastrointestinal tract, liver, and spleen, which are sites where OVCAR8 tumor cells frequently infiltrate.

In vivo antitumor efficacy study of CAR-NKT and CAR-T cells: OVCAR8-FG human OC xenograft NSG mouse model

On day 0, NSG mice were inoculated intraperitoneally with OVCAR8-FG human ovarian cancer cells (2×10^5 cells per mouse). Four days later, mice were randomly assigned to receive intraperitoneal administration of vehicle control (100 μ L PBS), CAR-NKT cells (1×10^7 CAR⁺ cells in 100 μ L PBS), CAR-T cells (1×10^7 CAR⁺ cells in 100 μ L PBS), or IL-15-enhanced CAR-T cells (1×10^7 CAR⁺ cells in 100 μ L PBS). CAR-T products were pre-sorted to enrich for CAR-expressing cells prior to infusion. Tumor progression was monitored by bioluminescence imaging twice weekly, and animals were followed longitudinally for survival.

In vivo antitumor efficacy study of CAR-NKT cells: SKOV3-FG human OC xenograft NSG mouse model

On day 0, NSG mice were intraperitoneally inoculated with SKOV3-FG human ovarian cancer cells (2×10^5 cells per mouse). On day 4, mice received intraperitoneal administration of vehicle control (100 μ L PBS), HSPC-derived CAR-NKT cells (1×10^7 CAR⁺ cells in 100 μ L PBS), or PBMC-derived CAR-NKT cells (1×10^7 CAR⁺ cells in 100 μ L PBS). PBMC-derived CAR-NKT cells were enriched for CAR expression by pre-sorting prior to infusion. Tumor burden was monitored by bioluminescence imaging twice weekly throughout the study, and animals were followed longitudinally for survival.

In vivo pharmacokinetics/pharmacodynamics (PK/PD) study of CAR-NKT/FG and CAR-T/FG cells: human OC xenograft NSG mouse model

On day 0, NSG mice were intraperitoneally inoculated with OVCAR8 tumor cells (2×10^5 cells per mouse). On the same day, mice received either intraperitoneal or intravenous administration of CAR-NKT/FG cells (1×10^7 CAR⁺ cells in 100 μ L PBS) or CAR-T/FG cells (1×10^7 CAR⁺ cells in 100 μ L PBS). Throughout the study, mice were monitored for survival, and therapeutic cell persistence was assessed twice weekly by BLI. In this model, only the therapeutic immune cells, not the tumor cells, were labeled with FG.

Longitudinal tracking of CAR-T and CAR-NKT cells was performed through serial sampling of peritoneal fluid and peripheral blood. Peritoneal lavage was conducted by injecting 500 μ L of sterile PBS into the peritoneal cavity, followed by gentle abdominal massage and recovery of lavage fluid using the same syringe. Peripheral blood was collected via retro-orbital bleeding under isoflurane anesthesia into EDTA-coated tubes for downstream analyses.

In vivo antitumor efficacy study of CAR-NKT and CAR-T cells combined with TIGIT blockade: OVCAR8-FG human OC xenograft NSG mouse model

On day 0, NSG mice were intraperitoneally implanted with OVCAR8-FG human ovarian cancer cells (5×10^5 cells per mouse). Four days later, mice received intraperitoneal infusion of CAR-NKT or CAR-T cells (1×10^7 CAR⁺ cells in 100 μ L PBS). Throughout the study, animals were treated with weekly doses of anti-TIGIT antibody (200 μ g in 100 μ L per mouse; Selleckchem, #A2033). Mice were followed longitudinally for survival, and tumor progression was assessed twice weekly using bioluminescence imaging.

In vivo antitumor efficacy study of CAR-T cells combined with PD-1 blockade: OVCAR8-FG human OC xenograft NSG mouse model

On day 0, NSG mice were intraperitoneally implanted with OVCAR8-FG human ovarian cancer cells (5×10^5 cells per mouse). Four days later, mice received intraperitoneal infusion of CAR-T cells (1×10^7 CAR⁺ cells in 100 μ L PBS). Throughout the study, animals were treated with weekly doses of anti-PD-1 antibody

(200 μ g in 100 μ L per mouse; pembrolizumab; Selleckchem, #A2005). Mice were monitored for survival, and tumor burden was assessed twice weekly by bioluminescence imaging.

In vivo antitumor efficacy study of CAR-NKT and CAR-T cells combined with CD96 blockade: OVCAR8-FG human OC xenograft NSG mouse model

On day 0, NSG mice were intraperitoneally inoculated with OVCAR8-FG human ovarian cancer cells (5×10^5 cells per mouse). On day 4, mice received intraperitoneal infusion of CAR-NKT or CAR-T cells (1×10^7 CAR⁺ cells in 100 μ L PBS). Throughout the study, animals were administered anti-CD96 antibody weekly (200 μ g in 100 μ L per mouse; Cell Sciences, #DHE25701B). Mice were monitored for survival, and tumor progression was assessed twice weekly using bioluminescence imaging.

Library preparation, single-cell RNA sequencing, and alignment
scRNA-seq was performed to characterize the in vivo transcriptional profiles of therapeutic cells, tumor cells, and host immune cells in an OVCAR8-FG human ovarian cancer xenograft model established in NSG mice. Two therapeutic cell products (i.e., CAR-T and CAR-NKT cells) were analyzed at five time points: day 0 (pre-infusion), and days 14, 28, 42, and 56 post-infusion. Day 0 samples were collected prior to cell administration, whereas post-infusion samples were isolated from tumor sites, peripheral blood, spleen, and liver. Tumor cells (OVCAR8-FG) and murine immune cells (mouse CD45⁺ cells) were collected on day 28.

For each experimental group, cells isolated from 10 mice were pooled for scRNA-seq analysis. Fresh samples were immediately transferred to the UCLA TCGB Core for library preparation. Cell concentrations were determined using a Countess II automated cell counter (Invitrogen/Thermo Fisher Scientific). Cells were loaded onto the Chromium Controller (10x Genomics), and single-cell libraries were generated using the Chromium Next GEM Single Cell 3' Kit v3.1 and Chromium Next GEM Chip G, following the manufacturer's protocols. Library quality was assessed using D1000 ScreenTape on a 4200 TapeStation System (Agilent Technologies). Sequencing was performed on an Illumina NovaSeq platform using the NovaSeq S4 Reagent Kit (100 cycles). Raw sequencing data were processed using the Cell Ranger software suite (10x Genomics), and individual samples were demultiplexed and aligned to generate a merged digital gene expression matrix via the Cell Ranger count pipeline.

Cell clustering and annotation

The expression matrix generated by Cellranger were analyzed using an R package Seurat (v4.2.2). Briefly, Seurat objects of individual samples were created using the feature, barcode, and matrix files from the Cellranger output. Then, individual Seurat objects were merged into one Seurat object. After filtering the low-quality cells, the expression matrix was normalized using NormalizeData function, followed by selecting variable features across datasets using FindVariableFeatures function and ScaleData function. To correct the batch effect, Harmony, an R package, was applied immediately after PCA, which was based on the combined matrix of the informative genes. Then Uniform Manifold Approximation and Projection (UMAP) and clustering were performed on the "harmony space" to identify clusters following the standard Seurat workflow for dimension reduction and clustering. To annotate the clusters, clusters of therapeutic cells were manually merged based on gene signatures reported from Human Protein Atlas (proteinatlas.org) and previous studies (GSE156728 and GSE122713). AddModuleScore function was used to calculate module scores of each list of gene signatures, and FeaturePlot function was used to visualize the expression of each signature in the UMAP plots. For GSEA, clusterProfiler packages were used to calculate the enrichment scores of each cluster in the signature gene list.

To benchmark our preclinical product against established clinical cell therapies, we integrated our scRNA-seq dataset with publicly available datasets from a phase I clinical trial employing anti-GD2 CAR-NKT cells armored with interleukin-15 (GSE154037 and GSE223071). Gene expression heatmap was generated with the function DoHeatmap. Differentially expressed genes were identified using the function FindMarkers by comparing CAR-NKT cells in vivo versus in vitro and GD2.CAR15-NKT cells post- versus pre-infusion. Pathway enrichment analysis was conducted in ShinyGO 0.82 with GO Biological Process pathway database.

Single-cell pathway analysis (SCPA)

Normalized cell-gene matrix was extracted from each relevant dataset. All pathways used in the analysis were generated from the publicly available molecular signatures database including The Molecular Signatures Database (MSigDB), Kyoto Encyclopedia of Genes and Genomes (KEGG), Reactome Pathway Database, BioCarta and Gene Ontology (GO): biological process. Comparisons were then performed using the compare_pathways function within SCPA. Data processing and visualization was then performed using Seurat, ggplot2, and ComplexHeatmap packages.

CytoTRACE analysis

Cell differentiation states were inferred from scRNA-seq data using CytoTRACE (Cellular Trajectory Reconstruction Analysis using gene Counts and Expression). Briefly, gene expression matrices for the relevant cell populations were extracted, retaining single-cell identifiers and corresponding gene expression values. These matrices were uploaded to the CytoTRACE web interface (<https://cytotrace.stanford.edu/>) to predict cellular differentiation states. CytoTRACE scores were computed for each cell and subsequently integrated back into the Seurat object corresponding to the scRNA-seq dataset. The scores were visualized on UMAP embeddings, and two-dimensional plots were generated using the FeaturePlot function in the Seurat R.

Pseudotime trajectory analysis

The R package dyno was used to calculate trajectories across pseudotime. Briefly, the top 1000 most variable genes were taken from CAR-T or CAR-NKT samples on day 28. Both the counts and normalized expression (with genes/features in columns) were used to create a wrapper object. After wrapping the data, the most optimized trajectory inference method was selected using a shiny app dynguidelines by calling the guidelines_shiny function. Afterwards, the trajectory of CAR-T or CAR-NKT cells was calculated using the infer_trajectory function within dyno, using the selected optimized method. Pseudotime of each cell along the trajectory was calculated using the calculate_pseudotime function within dyno and integrated back into the Seurat object of the scRNA-seq dataset and plotted on the UMAP afterward.

Statistical analysis

Statistical analyses were performed using GraphPad Prism 9 (GraphPad Software). Two-tailed Student's t tests were applied for pairwise comparisons. For analyses involving more than two groups, ordinary one-way ANOVA followed by Tukey's or Dunnett's multiple-comparisons tests was used, as appropriate. Survival curves were analyzed using the log-rank (Mantel-Cox) test with adjustment for multiple comparisons. Data are presented as mean \pm SEM unless otherwise specified. In all figures and figure legends, N denotes the number of biological samples or animals analyzed. A p value of less than 0.05 was considered significant. ns, not significant; * $p < 0.05$; ** $p < 0.01$; *** $p < 0.001$; **** $p < 0.0001$. For scRNA-seq analysis, p values of violin plots were determined by Wilcoxon rank sum test. For violin plot comparisons involving large datasets, P values were often extremely small (sometimes $< 2.2 \times 10^{-16}$). Therefore, a “#” symbol was placed above the indicated violin plots to denote statistical significance.

DATA AVAILABILITY

All data associated with this study are present in the paper or Supplementary Information. The genomics data generated during this study are available from the public repository Gene Expression Omnibus Database: GSE268749 (scRNA-seq for the in vivo therapeutic cell profiling study) and GSE255431 (scRNA-seq for the in vivo tumor cell profiling study). All animal experiments were approved by the UCLA Institutional Animal Care and Use Committee (IACUC) and conducted in accordance with guidelines from the UCLA Division of Laboratory Animal Medicine (DLAM). Healthy donor PBMCs were obtained from the UCLA Center for AIDS Research (CFAR) Virology Core Laboratory as de-identified specimens in accordance with US federal and state regulations.

ACKNOWLEDGEMENTS

We thank the University of California, Los Angeles (UCLA) animal facility for providing animal support; the UCLA Translational Pathology Core Laboratory (TPCL) for providing histology support; the UCLA Technology Centre for Genomics & Bioinformatics (TCGB) facility for providing RNA-seq services; the UCLA CFAR Virology Core for providing human cells; and the UCLA BSCRC Flow Cytometry Core Facility for cell sorting support. This work was supported by Partnering Opportunity for Discovery Stage Research Projects Awards and Translational Research Projects Awards from the California Institute for Regenerative Medicine (DISC2-11157, DISC2-13015, TRAN1-12250, and TRAN1-16050 to L.Y.), a Department of Defense CDMRP PRCRP Impact Award (CA200456 to L.Y.), a UCLA BSCRC Innovation Award (to L.Y.), and an Ablon Scholars Award (to L.Y.). L.Y. is a member of the Parker Institute for Cancer Immunotherapy, UCLA. Y.-R.L. is a postdoctoral fellow supported by a UCLA MIMG M. John Pickett Post-Doctoral Fellow Award, a CIRM-BSCRC Postdoctoral Fellowship, a UCLA Sydney Finegold Postdoctoral Award, a UCLA Chancellor's Award for Postdoctoral Research, and a Goodman-Luskin Microbiome Center Collaborative Research Fellowship award.

AUTHOR CONTRIBUTIONS

Y.-R.L., M.L., and Y.C. designed the experiments, analyzed the data, and wrote the manuscript. L.Y. conceived and oversaw the study, with assistance from Y.-R.L., and with suggestions from H.R.C. and A.J.L. Y.-R.L. and M.L. performed all experiments, with assistance from Y.C., H.L., Y.Z., X.S., D.C., E.Z., J.H., Y.-C.W., and A.S.K. All authors have read and approved the article.

ADDITIONAL INFORMATION

Supplementary information The online version contains supplementary material available at <https://doi.org/10.1038/s41392-026-02602-x>.

Competing interests: Y.-R.L. and L.Y. are inventors on patents relating to this study filed by UCLA. M.L. is currently an employee of AstraZeneca. L.Y. is a scientific advisor to AlzChem and Amberstone Biosciences, and a co-founder, stockholder, and advisory board member of Appia Bio. Appia Bio licensed some patents relating to this study from UCLA. None of the declared companies contributed to or directed any of the research reported in this article. The remaining authors declare no competing interests.

Publisher's note Springer Nature remains neutral with regard to jurisdictional claims in published maps and institutional affiliations.

REFERENCES

1. Dagher, O. K. & Posey, A. D. Forks in the road for CAR T and CAR NK cell cancer therapies. *Nat. Immunol.* **24**, 1994–2007 (2023).
2. Li, Y.-R., Zhu, Y., Fang, Y., Lyu, Z. & Yang, L. Emerging trends in clinical allogeneic CAR cell therapy. *Med* 100677 <https://doi.org/10.1016/j.medj.2025.100677> (2025).
3. Nelson, A., Lukacs, J. D. & Johnston, B. The current landscape of NKT cell immunotherapy and the hills ahead. *Cancers* **13**, 5174 (2021).
4. Hadiloo, K., Tahmasebi, S. & Esmaeilzadeh, A. CAR-NKT cell therapy: a new promising paradigm of cancer immunotherapy. *Cancer Cell Int.* **23**, 86 (2023).
5. Li, Y.-R. et al. Allogeneic CD33-directed CAR-NKT cells for the treatment of bone marrow-resident myeloid malignancies. *Nat. Commun.* **16**, 1248 (2025).
6. Li, Y.-R. et al. Engineering allojection-resistant CAR-NKT cells from hematopoietic stem cells for off-the-shelf cancer immunotherapy. *Mol. Ther.* <https://doi.org/10.1016/j.jymthe.2024.04.005> (2024).
7. Zhou, X. et al. CAR-redirected natural killer T cells demonstrate superior anti-tumor activity to CAR-T cells through multimodal CD1d-dependent mechanisms. *Nat. Cancer* <https://doi.org/10.1038/s43018-024-00830-0> (2024).
8. Heczey, A. et al. Invariant NKT cells with chimeric antigen receptor provide a novel platform for safe and effective cancer immunotherapy. *Blood* **124**, 2824–2833 (2014).

9. Kim, C. H., Johnston, B. & Butcher, E. C. Trafficking machinery of NKT cells: shared and differential chemokine receptor expression among Va24+Vβ11+ NKT cell subsets with distinct cytokine-producing capacity. *Blood* **100**, 11–16 (2002).
10. Wang, H. et al. Immune checkpoint blockade and CAR-T cell therapy in hematologic malignancies. *J. Hematol. Oncol.* **12**, 59 (2019).
11. Grosser, R., Cherkassky, L., Chintala, N. & Adusumilli, P. S. Combination immunotherapy with CAR T cells and checkpoint blockade for the treatment of solid tumors. *Cancer Cell* **36**, 471–482 (2019).
12. Suarez, E. R. et al. Chimeric antigen receptor T cells secreting anti-PD-L1 antibodies more effectively regress renal cell carcinoma in a humanized mouse model. *Oncotarget* **7**, 34341–34355 (2016).
13. Mittal, D. et al. CD96 is an immune checkpoint that regulates CD8(+) T-cell antitumor function. *Cancer Immunol. Res.* **7**, 559–571 (2019).
14. Kim, T.-J. et al. CD160 serves as a negative regulator of NKT cells in acute hepatic injury. *Nat. Commun.* **10**, 3258 (2019).
15. Li, Y.-R. et al. Protocol to profile tumor and microenvironment from ovarian cancer patient samples and evaluate cell-based therapy using in vitro killing assays. *STAR Protoc.* **6**, 103742 (2025).
16. Li, Y.-R. et al. Generation of allogeneic CAR-NKT cells from hematopoietic stem and progenitor cells using a clinically guided culture method. *Nat. Biotechnol.* <https://doi.org/10.1038/s41587-024-02226-y> (2024).
17. Heczey, A. et al. Anti-GD2 CAR-NKT cells in patients with relapsed or refractory neuroblastoma: an interim analysis. *Nat. Med.* **26**, 1686–1690 (2020).
18. Heczey, A. et al. Anti-GD2 CAR-NKT cells in relapsed or refractory neuroblastoma: updated phase 1 trial interim results. *Nat. Med.* <https://doi.org/10.1038/s41591-023-02363-y> (2023).
19. Gschwend, E., De Oliveira, S. & Kohn, D. B. Hematopoietic stem cells for cancer immunotherapy. *Immunol. Rev.* **257**, 237–249 (2014).
20. Giannoni, F. et al. Allelic exclusion and peripheral reconstitution by TCR transgenic T cells arising from transduced human hematopoietic stem/progenitor cells. *Mol. Ther.* **21**, 1044–1054 (2013).
21. Li, Y.-R. et al. Overcoming ovarian cancer resistance and evasion to CAR-T cell therapy by harnessing allogeneic CAR-NKT cells. *Med* 100804 <https://doi.org/10.1016/j.medj.2025.100804> (2025).
22. Li, Y.-R. et al. Managing allojection in off-the-shelf CAR-engineered cell therapies. *Mol. Ther.* <https://doi.org/10.1016/j.ymthe.2024.11.035> (2024).
23. Fang, Y. et al. Protocol to generate allojection-resistant universal CAR-NKT cells and evaluate their efficacy, mechanism of action, safety, and immunogenicity. *STAR Protoc.* **6**, 103810 (2025).
24. Liu, Y., Sperling, A. S., Smith, E. L. & Mooney, D. J. Optimizing the manufacturing and antitumor response of CAR T therapy. *Nat. Rev. Bioeng.* **1**, 271–285 (2023).
25. Rafiq, S., Hackett, C. S. & Brentjens, R. J. Engineering strategies to overcome the current roadblocks in CAR T cell therapy. *Nat. Rev. Clin. Oncol.* **17**, 147–167 (2020).
26. Larson, R. C. & Maus, M. V. Recent advances and discoveries in the mechanisms and functions of CAR T cells. *Nat. Rev. Cancer* **21**, 145–161 (2021).
27. Haas, A. R. et al. Two cases of severe pulmonary toxicity from highly active mesothelin-directed CAR T cells. *Mol. Ther.* **31**, 2309–2325 (2023).
28. Baeyens, A., Fang, V., Chen, C. & Schwab, S. R. Exit strategies: S1P signaling and T cell migration. *Trends Immunol.* **36**, 778–787 (2015).
29. Kohli, K., Pillarisetty, V. G. & Kim, T. S. Key chemokines direct migration of immune cells in solid tumors. *Cancer Gene Ther.* **29**, 10–21 (2022).
30. Beziat, V. et al. Shaping of iNKT cell repertoire after unrelated cord blood transplantation. *Clin. Immunol.* **135**, 364–373 (2010).
31. Li, Y.-R., Zhu, Y. & Yang, L. IL-15 in CAR engineering: striking an efficacy-safety balance. *Trends Mol. Med.* <https://doi.org/10.1016/j.molmed.2025.05.014> (2025).
32. Giavridis, T. et al. CAR T cell-induced cytokine release syndrome is mediated by macrophages and abated by IL-1 blockade. *Nat. Med.* **24**, 731–738 (2018).
33. Steffin, D. et al. Interleukin-15-armed GPC3 CAR T cells for patients with solid cancers. *Nature* <https://doi.org/10.1038/s41586-024-08261-8> (2024).
34. Good, C. R. et al. An NK-like CAR T cell transition in CAR T cell dysfunction. *Cell* **184**, 6081–6100.e26 (2021).
35. Bendelac, A., Savage, P. B. & Teyton, L. The biology of NKT cells. *Annu. Rev. Immunol.* **25**, 297–336 (2007).
36. Kumar, A. et al. Natural killer T cells: an ecological evolutionary developmental biology perspective. *Front. Immunol.* **8**, 1858 (2017).
37. Jin, S. et al. Inference and analysis of cell-cell communication using CellChat. *Nat. Commun.* **12**, 1088 (2021).
38. Chiang, E. Y. & Mellman, I. TIGIT-CD226-PVR axis: advancing immune checkpoint blockade for cancer immunotherapy. *J. Immunother. Cancer.* **10**, e004711 (2022).
39. Archilla-Ortega, A., Domuro, C., Martin-Liberal, J. & Muñoz, P. Blockade of novel immune checkpoints and new therapeutic combinations to boost antitumor immunity. *J. Exp. Clin. Cancer Res.* **41**, 62 (2022).
40. Li, Z. et al. Therapeutic application of human type 2 innate lymphoid cells via induction of granzyme B-mediated tumor cell death. *Cell* **187**, 624–641.e23 (2024).
41. Li, S. et al. Engineering an in vivo charging station for CAR-redirection invariant natural killer T cells to enhance cancer therapy. *Res. Sq.* <https://doi.org/10.21203/rs.3.rs-6215345/v1> (2025).
42. Li, Y.-R. et al. Development of allogeneic HSC-engineered iNKT cells for off-the-shelf cancer immunotherapy. *Cell Rep. Med.* **2**, 100449 (2021).
43. Wang, Z. et al. 3D-organoid culture supports differentiation of human CAR+ iPSCs into highly functional CAR T cells. *Cell Stem Cell* **29**, 515–527.e8 (2022).
44. Seet, C. S. et al. Generation of mature T cells from human hematopoietic stem and progenitor cells in artificial thymic organoids. *Nat. Methods* **14**, 521–530 (2017).
45. Kronenberg, M. Toward an understanding of NKT cell biology: progress and paradoxes. *Annu. Rev. Immunol.* **23**, 877–900 (2005).
46. Bae, E.-A., Seo, H., Kim, I.-K., Jeon, I. & Kang, C.-Y. Roles of NKT cells in cancer immunotherapy. *Arch. Pharm. Res.* **42**, 543–548 (2019).
47. Wang, Y. & Li, Y.-R. Harnessing chimeric antigen receptor-engineered invariant natural killer T cells: therapeutic strategies for cancer and the tumor microenvironment. *Curr. Pharm. Biotechnol.* **25**, 2001–2011 (2024).
48. Li, Y.-R. et al. Off-the-shelf third-party HSC-engineered iNKT cells for ameliorating GvHD while preserving GvL effect in the treatment of blood cancers. *iScience* **25**, 104859 (2022).
49. Diorio, C., Teachey, D. T. & Grupp, S. A. Allogeneic chimeric antigen receptor cell therapies for cancer: progress made and remaining roadblocks. *Nat. Rev. Clin. Oncol.* **22**, 10–27 (2025).
50. Lyu, Z. et al. Addressing graft-versus-host disease in allogeneic cell-based immunotherapy for cancer. *Exp. Hematol. Oncol.* **14**, 66 (2025).



Open Access This article is licensed under a Creative Commons Attribution 4.0 International License, which permits use, sharing, adaptation, distribution and reproduction in any medium or format, as long as you give appropriate credit to the original author(s) and the source, provide a link to the Creative Commons licence, and indicate if changes were made. The images or other third party material in this article are included in the article's Creative Commons licence, unless indicated otherwise in a credit line to the material. If material is not included in the article's Creative Commons licence and your intended use is not permitted by statutory regulation or exceeds the permitted use, you will need to obtain permission directly from the copyright holder. To view a copy of this licence, visit <http://creativecommons.org/licenses/by/4.0/>.

© The Author(s) 2026